HARVARD
Kenneth C. Griffin

GRADUATE SCHOOL
OF ARTS AND SCIENCES

DISSERTATION ACCEPTANCE CERTIFICATE

The undersigned, appointed by the

Harvard John A. Paulson School of Engineering and Applied Sciences
have examined a dissertation entitled:

"Optogenetic control and monitoring of ion transport in cells"

presented by: Rebecca Frank Hayward

Signature _____
Typed name: Professor Jennifer Lewis

Signature _____
Typed name: Professor Adam Cohen

Signature _____
Typed name: Professor Nicholas Bellono

Signature _____
Typed name: Professor Daniel Needleman

Date: September 16, 2024

Optogenetic control and monitoring of ion transport in cells

Rebecca Frank Hayward 09-16-2024

Rebecca Frank Hayward

Dissertation Advisor: Adam Cohen

Optogenetic control and monitoring of ion transport in cells

Abstract

Ion transport is a dynamic process that is important in signaling both between and within cells. Fluorescence-based measurements are well suited for investigations of ion transport due to their high sensitivity and high spatiotemporal resolution. Optogenetic actuators can locally perturb ion concentrations via combined optical and genetic targeting. Here we combine spectrally separate optogenetic control and monitoring to probe ion transport within cells. We apply these tools in neurons where ionic signals play many important roles across a wide range of space and time scales.

In Chapter 2 I investigate the effect on the intracellular pH of repeated neuronal stimulation with a blue-shifted optogenetic actuator, CheRiff, as measured with a red-shifted fluorescent pH sensor, pHoran4. We found that repeated CheRiff stimulation acidified neurons. The acidification was due to the channelrhodopsin CheRiff passing a proton current into the cell. To reduce this acidification, we characterized new channelrhodopsin variants with low proton permeability, and showed that they reduced the neuronal acidification and are viable alternatives for neuron stimulation.

In Chapter 3 I investigate diffusion of Ca^{2+} in dendrites, by combining a blue-shifted Ca^{2+} selective channelrhodopsin, CapChR2, with a red shifted fluorescent Ca^{2+} sensor, FR-GECO1c. Using patterned optical stimulation, we created small Ca^{2+} point sources in the dendrites of cultured neurons and imaged the diffusion of the Ca^{2+} ions along the dendrite. After the system reached steady-state characterized the length constants of the Ca^{2+} spread through the dendrites. We then did a paired measurement mapping the kinetic responses of the neuron cell body and dendrites to short wide-area Ca^{2+} perturbations. By combining this spatial and kinetic data, we estimated the effective diffusion coefficient for Ca^{2+} in

dendrites. We then investigated the effects of Ca^{2+} efflux on Ca^{2+} spread and kinetics. We added a pharmacological blocker of NCX1 sodium-calcium exchanger and repeated the Ca^{2+} transport and homeostasis measurements. These experiments showed that the NCX1 exchanger had a larger effect on calcium handling in fine dendrite than near the cell body, an effect that could be explained by the difference in surface-to-volume ratio of these structures.

Finally, I discuss other optogenetic actuators and reporters that could be combined for control and monitoring of different signals of interest. I discuss the factors for choosing what tools to use together and how to ensure the proper functioning and interpretation. As more optogenetic actuators and reporters are created, there are ever more possibilities for probing important signaling pathways. However, it is also important to make sure that the molecular and optical tools are well understood and validated, as there can be artifacts which can affect cellular state and which may confound results, as seen in Chapter 2.

Table of Contents

Acknowledgements

I’m extremely grateful to my advisor, Adam Cohen, for taking a chance on me as a fresh graduate student with no experience in biology and helping to give me the opportunity and push to learn and grow over my PhD. I am also grateful to my lab mates who have provided a lot of learning and support both academically and personally. I’d also like to acknowledge my family and friends who have always believed in me and kept me going. Lastly, I could not have undertaken this journey without my partner, Woody, who has done so much to ensure that I was successful and keep me going.

Dedication

To myself for always reaching for more, and my partner for helping me do so.

List of Figures

List of Tables

Chapter 1 Introduction

1.1 Cellular Signaling

Cellular compartments communicate with each other through intracellular signaling. For example, receptors on the membrane activate a variety of signaling pathways to convey information from the extracellular surface to the rest of the cell. These pathways include ion-mediated signals, as well as second messengers and signaling cascades for G-protein coupled receptors (GPCRs) and receptor tyrosine kinases (RTKs). Intracellular signaling pathways control aspects of the cell such as metabolism, transcription and translation, and cell state. Many signaling pathways share a few second messengers: different receptors can cause different effects even though they use the same small molecule or ion for signaling[1–3]. This multiplexing is achieved by spatial confinement of the signaling molecules to different subcellular domains. This localization motivates in-depth analyses of signaling pathways in space and time, to understand how different responses are obtained by control of the spatiotemporal patterns of intracellular signaling.

Adjacent cells can couple to each other via gap junction connections, which form channels through which signals can propagate. A gap junction-coupled layer of cells can have different properties than individual cells. In one example, we showed that two groups of cells which individually could not create action potentials, when grown in adjacent regions and coupled by gap junction connections, supported action potentials along the contact boundary[4]. For signals that can spread across many cells, such as voltage, tissue-scale gradients can form. These signals can be hard to see on the scale of individual cells, and signals can propagate far from where they originate. Techniques that look at individual cells are insensitive to these effects, as they are blind to the signals that are coming from other cells. An important area of study in cellular signaling is to identify and characterize the qualitatively new emergent properties that come from ensembles of coupled cells.

Many diseases originate from improper signaling. Gap junctions have been shown to be relevant in epilepsy[5], as well as in neurodegenerative diseases[6]. Membrane channels are implicated in diseases for

example calcium channelopathies include at least 7 disorders, including retinal abnormalities, migraines, and ataxia[7]. Receptor Tyrosine Kinases (RTKs) are involved in diseases such as cancer, as well as atherosclerosis, diabetes, and many different developmental disorders[8]. G-protein coupled receptors (GPCRs) are also involved in diseases ranging from metabolic, immunological, and neurodegenerative disorders, to cancer and infectious diseases. 40% of clinically used drugs modulate GPCRs[9,10]. For us to better understand these disease states and how to fix them, we need to study cellular signaling.

1.1.1 Measuring Cellular Signaling

Signals are dynamic and change over space and time. There are many different techniques which are used to assess these signals, each with their own advantages and disadvantages.

Traditional biochemical assays such as western blots, immunoprecipitation, and pull-down assays have long been used to assess interactions between proteins[11]. These are useful for discovering signaling pathways and how they interact and are activated, but they are endpoint measurements, as cells are destroyed to take the measurement. This means that it can be challenging to get timing information. As bulk measurements, these techniques also often average over possibly heterogeneous cellular populations. Disruption of the sample also typically destroys spatial information.

Techniques for massively parallel measurements, termed “omics”, such as transcriptomics[12] and proteomics[13] have recently become popular. These techniques are useful for discovering different cells that may interact via signaling pathways, and even signaling interactions within a single cell. However, these techniques are also usually endpoint measurements which suffer the same problems previously mentioned. Additionally, these measurements give the presence but not the conformational state of proteins and genes, so we don’t know their activity, just their abundance.

Electrical signals can be measured via electrodes. Arrays of extracellular electrodes[14] can give some spatial information but do not probe the membrane voltage directly. Electrodes attached to a single cell, called patch clamp electrophysiology, directly probe the membrane voltage, but typically are not highly parallelized[15].

1.1.2 Fluorescent reporters

Fluorescence-based techniques have been very useful for performing measurements with high space and time resolution. Most cells are not intrinsically responsive to light, so fluorescence measurements can be relatively non-perturbative. Optical techniques are adaptable over many spatial scales, so that fluorescence imaging can be used to measure intracellularly and/or over large areas. This flexibility is particularly useful for neuroscience, where we may want to image over large collections of neurons working together.

Fluorescent recovery after photobleaching (FRAP) has been used with dyes for a long time, as well as more recently with fluorescent proteins (FPs), to look at the diffusion and movement of proteins within cells[16]. The drawback of this technique is that it does not necessarily reflect the motion of signaling events, but just normal diffusion of the signaling substrate.

A useful technique for measuring interactions of proteins is fluorescence resonance energy transfer (FRET) which measures when two fluorophores are within <100 Å of each other[17]. This technique gives the ability to observe protein interactions and binding events with great space and time resolution. The drawback of this technique is that two fluorophores must be used and attached to the components that are proposed to interact, without changing their ability to bind.

In general, fluorescent proteins (FPs) fused to proteins of interest through genetic manipulations are very useful for imaging changes in the location and concentration of proteins over time. There are many signals which can cause proteins to translocate to the membrane or nucleus, and this can be easily measured using fluorescence.

Fluorescent proteins have also been developed into fluorescent sensors, by using domains that bind signaling molecules and alter the fluorescence of the fused FPs. This approach is useful for investigating the intracellular changes in signaling molecules as well as macroscopic changes over many cells. One limitation of fluorescent techniques are the broad spectra of many fluorescent molecules, which limit the number of probes that can be used simultaneously. However, many sensors for different molecules have been and continue to be created, expanding the toolbox of possible probes of signaling in cells.

1.2 Neuronal Signaling

Ramon y Cajal established the neuron as the fundamental unit of the brain[18,19], which can communicate signals through electrical activity known as action potentials or spikes as discovered by Julius Bernstein, with the help of Emil du Bois-Reymond[20].

Action potentials in neurons are the result of the opening and closing of membrane channels which cause a flux of ions across the membrane[21]. These ions fluxes change the membrane potential, which is one of the main signal carriers in neurons. Action potentials can be triggered by cellular interactions and can trigger other signals such as voltage gated calcium channels for an influx of calcium. Action potentials also signal through neurotransmitter release, which transmits signals to other cells across synapses.

This signaling is important across many spatial scales in the brain. While neurons are often considered the fundamental unit of the brain, they have a complex morphology with features such as dendrites and spines. This interesting geometry can create sub-cellular differences in their signals and electrical activity. For example, dendrites may have different voltages than their soma[22]. Small groups of neurons, i.e. microcircuits, may also have collective patterns of electrical and chemical signaling[23]. Whole brain regions also have interesting electrical and chemical signaling patterns which evolve as the brain performs various types of tasks and processes different types of information[24].

Signaling in neurons also goes across many temporal scales. While individual spikes in neurons last milliseconds, signals such as calcium transients typically last 100s of milliseconds. There are also important signals in neurons that could be changing on much longer time scales, such as alterations in transcription which happen on the scales of minutes to hours. Diverse signals are created by altering the frequency, kinetics, and durations of signaling events. This timing is important, as problems with synchronization can cause diseases such as epilepsy[25].

The broad range of space and time scales in the brain makes neuroscience challenging. Measurement techniques are typically optimized for a particular spatial and temporal scale, such as using biochemical assays for looking at signaling pathways and proteins; or using transcriptomics methods for looking at

transcription and genes, but these techniques are not good at measurements over time. Electrophysiology techniques like patch clamp can be useful for looking at electrical signaling in single cells with high temporal resolution and have been transformative for understanding electrical signals in neurons[15]. However, patch clamp lacks spatial information. Fluorescent techniques are useful in neuroscience for their ability to go across scales in space and time.

1.2.1 Calcium Signaling

Cells use calcium for many distinct signaling functions. Through calcium's role as a second messenger, it can have diverse spatial and temporal scales of signaling and affect many different processes. In neuroscience, cytoplasmic calcium concentration is often used as a proxy for neural firing, whereas the electrical signals are much faster and harder to measure. Fluorescent sensors of calcium have been used since 1980[26], starting as dyes that were inserted into cells[27]. One of the first protein based calcium sensors was aequorin[28,29] which led to the development of modern genetically encoded calcium indicators, such as cameleon in 1997[30]. Currently families of calcium indicators such as GCaMPs[31] have been developed to be as good or better than common calcium indicator dyes such as Oregon Green BAPTA. Spectral ranges of calcium indicators have also increased. The development of genetically encoded red-shifted calcium indicators such as R-GECO[32] and RCaMP[33] or the recently developed FR-GECO[34].

1.2.2 Neuron specific geometry

Neurons are famous for their iconic morphology. A neuron is generally composed of a soma which is the main cell body, containing nucleus and other organelles. Coming off the soma are dendrites which are long thin protrusions which branch into the dendritic arbor. These dendrites connect to the axons of other cells via synapses which are tiny spaces between the two in which neurotransmitters can be transmitted. The axons of presynaptic cells usually connect onto dendritic spines, which are small compartments coming out of the dendrite. These parts come together to make a complex system with compartments of varying size and geometry. This morphology has been shown to be important, as it can affect signaling such as the velocity and amplitude of back-propagating action potentials[35]. While the soma is the largest-volume compartment and is the most often measured, the dendrites are also active and can display

different types of dendritic information processing[36–38]. Because of the thin and spread-out morphology of dendrites, they have historically been difficult to measure, but as fluorescent sensors and methods have become better, the ability to measure and study the signaling happening within dendrites is well within grasp.

1.3 All-Optical Methods

As discussed previously, optical methods give spatial and temporal resolution across many different scales. Visible light can be used down to the diffraction limit, about 200 nm, which is much smaller than the diameter of an average cell at 10 μm, as well as up to the size of galaxies as used in telescopes. We also have light sources, cameras, and other readout device which can have fast time scales that are only limited by the electronic readout time of the system, down to μs. The light sources available today produce stable light for an almost unlimited amount of time. Because of the availability of advanced optoelectronics, the advent of genetic tools that are optically responsive has been hugely useful and continues to see a lot of development. The ability to combine optical readout with optical perturbation to create all-optical methods is in its infancy, but will no doubt see much expansion in the future.

1.3.1 Optogenetic actuators

Patch clamp electrophysiology measurements have been so useful for neuroscience because they give the ability to stimulate the neuron and to measure the response. Electrodes have also been used to stimulate large regions of the brain for observation of effects on overall neural functioning. Electrode-based tools lack the precise control for stimulation of subsets of cells, or subcellular stimulation. Genetic manipulations can be precisely targeted in space but lack fine temporal control. To combine the ideas of genetic manipulation with pharmacology, chemogenetic techniques such as designer receptors exclusively activated by designer drugs (DREADDs) were created[39]. Because of the necessity of addition of drugs, these techniques are also limited in temporal resolution, and typically lack sub-cellular spatial resolution. Stimulation of neurons by the addition of drugs or other small molecules is also limited in precision both in space and time. The ability to make precise perturbations to a system greatly enables the ability to develop and test signaling and to better understand how neurons function. Again, optics is advantageous for the control it provides in space and time.

One of the early optical actuators was caged glutamate, which could be optically uncaged using UV or two photon light. This glutamate uncaging could be used to stimulate neurons, but was difficult to use and unreliable due to it requiring exogenous materials which could become depleted, and it could be challenging to get high enough concentrations. Glutamate uncaging was combined with calcium sensors to create an early all-optical system[40]. Pairing of ionotropic receptors with photocaged ligands[41] was also tried, but the requirement for multiple components made it technically challenging.

The field of optogenetics began in 2005 when Channelrhodopsin2 (ChR2) was first used in neurons[42]. ChR2 is a blue light activated microbial rhodopsin and has become the most widely used optical actuator. It is a membrane channel which when opened with light can pass ions and thus have a depolarizing effect in polarized cells such as neurons. ChR2 is useful because of the ability to genetically target it to specific cell types and subpopulations and to be able to have the advantages of light microscopy's resolution in space and time. ChRs have been developed to become faster, sensitive to different wavelengths, and have larger photocurrents. They have become widely useful in many fields such as developmental biology[43], pharmacological screening[44], and cancer biology[45]. They are widely used in neuroscience[46–48], where they have been applied to understanding mood disorders[49,50], addiction[51], social behavior[52], and reward[53].

In addition to actuators causing neurons to spike, optical silencers of neurons were also developed, such as the proton pump Archarerhodopsin-3[54], chloride pump Halorhodopsin[55], anion channelrhodopsins known as GtACRs[56], and light-gated potassium channels[57]. Novel optical actuators continually expand the tools we have for exploring signaling and enable greater control, both for basic research applications and for clinical applications, such as in restoration of vision[58], and treatment of disorders of neural excitability[59].

As the number of variants and the types of use cases expands, it is important to have an accurate understanding of what these tools are doing, to interpret results accurately, and to ensure safety for possible clinical applications. It is important to understand, in the case of ChR, what ions are being passed and what effects these can have for the stimulation protocols that will be used. For example,

similar ChR variants have been reported to have opposite behavioral effects in mice due to unknown causes[60].

1.3.2 Combining optical actuators and reporters

While many advances have been made by using genetically targeted optical sensors and actuators, their simultaneous use enables many new kinds of experiments. For example, the combination of optical sensors and actuators can be used to create closed-loop systems.

There has been much work since the discovery of channelrhodopsins on combining ChRs with Ca^{2+} sensors[33,61–66]. When used in neurons, stimulating the ChR can evoke neural firing, which then activates voltage-gated calcium channels, which lead to an increase in calcium concentration. However, the indirect relation between ChR stimulation and calcium increase makes interpretation difficult. With the advent of red-fluorescent protein-based voltage sensors, our lab created 'optopatch', an all-optical system for simultaneous optical perturbation and measurement of membrane voltage. Optopatch can do measurements like in patch clamp electrophysiology, but with spatial resolution on the stimulation and measurement[67]. Recently the Optopatch system has become robust enough for use *in vivo*, in awake animals[68,47,69]. Optopatch has been useful for the ability to give precise characterization of neural circuits and to establish causal roles of specific components.

Another interesting all-optical system that our lab recently developed is 'cAMP-SITES' for optically targeted perturbation and measurement of cAMP[70]. Using a photoactivated adenylyl cyclase from the bacteria Beggiotoa[71] we directly stimulated the production of cAMP in cells with pulses of blue light. This actuator was combined with a red shifted sensor of cAMP, called 'Pink Flamindo'[72] for an all-optical cAMP system. The spatial pattern of cAMP signaling has been proposed to play a key role in its signaling specificity[73–75], however the estimates of cAMP diffusion in cells have varied by ~100 fold[76,77]. Using this all-optical cAMP system, we probed cAMP transport across many length scales and found a diffusion coefficient of 120 $\mu m^2/s$ in MDCK cells and neurons, and a length constant of 30 μm in the dendrites of neurons.

As more optogenetic actuators are created, we will be able to perturb and measure more signaling pathways with high resolution in space and time. This capability is useful for creating models of signaling,

understanding downstream signaling effects, and may eventually be combined with other techniques such as transcriptomics to determine gene functions[78].

1.4 Hardware and Software

As discussed above, an advantage of optogenetic actuators is that they can be activated in precise patterns in space and time. A digital micromirror device (DMD) is used to pattern light by electronic control over the tiny, arrayed mirrors. Patterns can be digitally transmitted to the DMD to create a binary mask, which is imparted to an incident beam of light by reflection. This optical patterning is used to stimulate specific subsets of cells in a sample, or subcellular regions within a cell.

I used a custom microscope shown in Figure 1. This system has lasers of 6 different wavelengths, which are combined into one optical path. Five of the lasers go through the Acousto-Optical Tunable Filter (AOTF) for dynamic control of laser intensities and switching between wavelengths, under control of the digital acquisition device (DAQ). The selected laser beams then reflect off the DMD to achieve precise spatial patterning. The 635 nm lasers are on a separate path which does not go through the AOTF or off of the DMD, because these lasers are typically used for wide-field illumination. After the DMD, all of the lasers are combined onto one path which goes into the objective and onto the sample. When doing voltage imaging, the 635 nm lasers can be used for wide-area fluorescence excitation, while the DMD is used to pattern optogenetic stimulation from the other lasers. For wide-area imaging and patterned stimulation with lasers that both go through the DMD path, we rapidly and synchronously alternated the illumination wavelength and the DMD pattern, to achieve independent patterns at different wavelengths. The DAQ and DMD, as well as all other electronic devices, are controlled through a software platform created in the lab, Luminos[79].

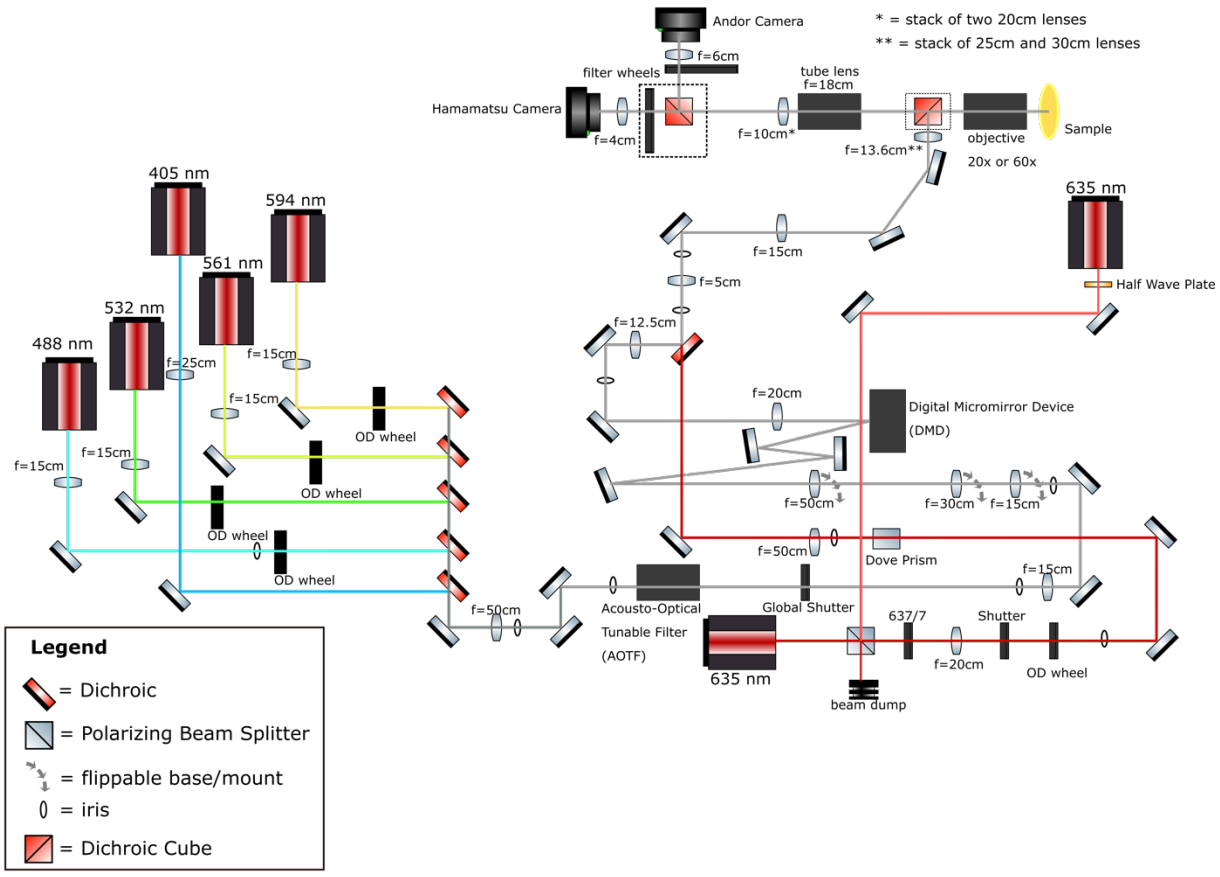

Figure 1: Optical diagram of custom microscope setup.

1.5 Summary

The combination of optogenetic control and monitoring shows promise for measurements of signaling, but these can also have unintentional effects and perturbations. In Chapter 2 I show measurements of neurons using ChR stimulation in combination with pH measurements. This work showed that repeated stimulation using the ChR CheRiff acidifies cells. We identify proton currents through the ChR as the cause of the acidification and characterize new ChRs with low proton permeability as alternatives for optogenetic stimulation. In Chapter 3 I use optogenetic control and monitoring of Ca^{2+} in the dendrites of neurons to map the spatial spread and kinetics of response to perturbations. Using repeated paired measurements in cells we calculate the effective diffusion coefficient for Ca^{2+} in dendrites of neurons.

Lastly, in Chapter 4 I discuss the future of optogenetics with other optogenetic tools, and how to create all-optical systems, and the use of optogenetics in drug development.

Chapter 2 Diminishing neuronal acidification by channelrhodopsins with low proton conduction

2.1 Abstract

Many channelrhodopsins are permeable to protons. We found that in neurons, activation of a high-current channelrhodopsin, CheRiff, led to significant acidification, with faster acidification in the dendrites than in the soma. Experiments with patterned optogenetic stimulation in monolayers of HEK cells established that the acidification was due to proton transport through the opsin, rather than through other voltage-dependent channels. We identified and characterized two opsins which showed large photocurrents, but small proton permeability, PsCatCh2.0 and ChR2-3M. PsCatCh2.0 showed excellent response kinetics and was also spectrally compatible with simultaneous voltage imaging with QuasAr6a. Stimulation-evoked acidification is a possible source of disruptions to cell health in scientific and prospective therapeutic applications of optogenetics. Channelrhodopsins with low proton permeability are a promising strategy for avoiding these problems.

2.2 Introduction

Channelrhodopsins are light-gated ion channels that are widely used to modulate the activity of neurons and other excitable cells.[80] In addition to research use, these tools are entering clinical practice as a treatment for forms blindness[81,82] and are under consideration for treatments of other disorders of neural excitability.[83–85] Every ion channel carries current through one or more ions, and so the induced change in membrane voltage is always accompanied by a change in ionic concentrations. In both research and clinical applications, one must consider whether the ionic changes in the cell have effects beyond the purely electrical effects of the channel.

Ionic perturbations are largest when (a) the basal intracellular concentration of the relevant ion is low, (b) the surface-to-volume ratio is high and (c) the channel is activated chronically. Sodium, potassium, and chloride ion concentrations in cells are typically in the millimolar range, and thus the fractional changes in concentration of these ions due to channel opening are typically < 1%. In contrast, protons and calcium ions have low free concentrations, typically ~100 nM or lower. In these cases, the ionic fluxes due to channel opening can substantially perturb the concentration.

The amount of charge flux required to change membrane voltage by a given amount is proportional to the capacitance, and hence the membrane surface area. This charge is diluted into the volume. For this reason, ionic concentrations in small structures with high surface-to-volume ratios are more labile to optogenetic perturbations than are concentrations in large structures. One must therefore consider whether optogenetic tools substantially perturb ionic concentrations in thin structures such as axons, dendrites, or spines. Finally, ionic concentrations equilibrate much more slowly than does membrane potential. Brief optogenetic stimuli may have negligible effects on concentrations, whereas chronic stimuli with high duty cycle may have cumulative effects. Concerns about long-term consequences of optogenetic stimulation are particularly relevant to prospective therapeutic applications, where the tools may be used over long times in patients.

Channelrhodopsins have been shown to acidify cells, while light-driven outward proton pumps, such as Archaerhodopsin 3, alkalize cells.[86,87] Indeed, optogenetically triggered alkalization has been proposed as a tool to control cell death.[88] Intracellular acidification can suppress neuronal excitability and also suppress vesicle release,[89–91] but has also been reported to enhance release of adenosine[92,93] and dopamine.[94] Changes in intracellular pH can also affect cell differentiation[95] and metabolism[96] and survival.[86,87,90,97] Nominally similar channelrhodopsins have been reported to evoke opposite behavioral effects in live mice[60]. The cause of these differences is not known, but it is possible that these differences could be due, in part, to differences in ionic selectivity.

For these reasons, it is important to quantify and ultimately minimize perturbations to cellular pH from optogenetic tools. We combined channelrhodopsin stimulation with a red-shifted fluorescent pH sensor, pHoran4,[98] for measurement of pH changes during optogenetic stimulation. We used patterned

optogenetic stimulation in gap junction-coupled cellular monolayers to establish that the acidification was due to proton flux directly through the channelrhodopsin. We then tested two new opsins, ChR2-3M and PsCatCh2.0,[99] with a low proton permeability and found minimal perturbations to cellular pH. We performed a detailed electrophysiological and photophysical characterization of these opsins and showed that they are compatible with simultaneous voltage imaging. The new opsins may be promising for clinical applications where acidification is undesirable.

2.3 Results

2.3.1 CheRiff acidifies neurons

We developed lentiviral constructs and optical stimulus protocols for simultaneous optogenetic stimulation and pH measurements (Figure 2A). For the actuator we used CheRiff-GFP, a non-selective cation channel with an activation peak at 460 nm.[100] For the pH measurement we used pHoran4,[98] a red-shifted reporter with an excitation peak at 547 nm and a pK_a of 7.5. We calibrated the pH response of pHoran4 in permeabilized HEK293T (HEK) cells and in cultured neurons (Methods; Figure 3) and then used this calibration to convert changes in fluorescence to changes in pH (Figure 2B).

We imaged pH changes in cultured neurons during CheRiff stimulation. We alternated epochs of optogenetic stimulation (488 nm, 400-800 mW cm^{-2}, 0.5 s) and pH imaging (561 nm, 100-200 mW cm^{-2}, 1 s) to avoid crosstalk of the blue light into the pH recordings (Figure 2C). The pH dynamics were much slower than 1.5 s, so this process did not sacrifice information.

After 150 s of stimulation and imaging, the pH had decreased within the neurons that expressed CheRiff-GFP, from 7.3 to 6.76 ± 0.35 (mean ± S.D., *n* = 34 cells, Figure 2D, E), corresponding to an approximately 3-fold increase in concentration of free protons. We then measured the pH recovery for an additional 150 s without optogenetic stimulation (Figure 2E). Recovery was slow, returning to only pH 6.95 ± 0.33 (mean ± S.D.) after 150 s. Control experiments in neurons that expressed pHoran4 but not CheRiff showed a small fluorescence increase during the stimulation period (0.11 $\Delta F/F$), much smaller in magnitude and

opposite in sign compared to the change in cells expressing CheRiff and pHoran4 (-0.34 ΔF/F). This photo-artifact was subtracted from all recordings prior to analysis.

We observed that stimulation-induced pH changes and post-stimulation recovery were faster in the dendrites than in the soma (Figure 2G). This effect is most likely due to the higher surface-to-volume ratio of thin processes. For a given proton current density across the membrane, the change in local proton concentration is greater in a thin tube than in the large soma.

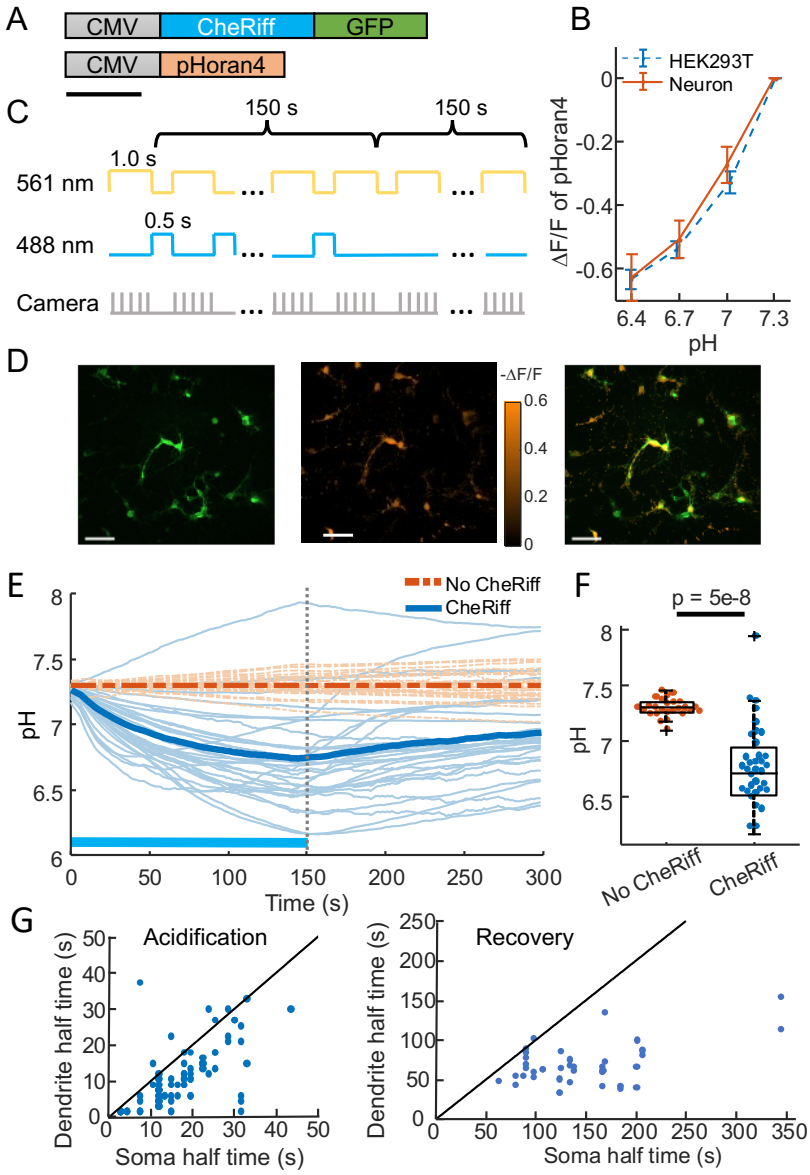

Figure 2: CheRiff acidifies polarized cells.

A) Genetic constructs for simultaneous optogenetic stimulation and pH imaging. B) Calibration of pHoran4 pH sensor in HEK cells and neurons. Error bars represent S.D. of n = 8 measurements in HEK cells, 42 measurements in neurons. C) Protocol for measuring pH responses to optogenetic stimulation. Stimulation (blue) and measurement (yellow) were interleaved for 150 s; then pH recovery was measured for 150 s without optogenetic stimulation. D) Example images of cultured neurons showing (left) GFP fluorescence, a marker for CheRiff expression, (middle) -ΔF/F in the pHoran4 channel after 150 s of the protocol shown in (C), (right) merge. Scale bars 100 μm. E) Time-course of pH in cultured neurons. Cells expressing pHoran4 but not CheRiff did not acidify. Bold lines show population average. F) CheRiff-expressing neurons acidified to a pH of 6.76 ± 0.35 (mean ± S.D., n = 34 cells). Neurons not expressing CheRiff had significantly less acidification, pH = 7.3 ± 0.08 (mean ± S.D., n = 26 cells, p = 5e-8 Wilcoxon rank sum test). Box plots show inter-quartile ranges, tick-marks show data range, + shows outlier. G) Half-time of (left) acidification or (right) recovery for neuron somas vs dendrites stimulated with the protocol in (C). Black line shows equal kinetics.

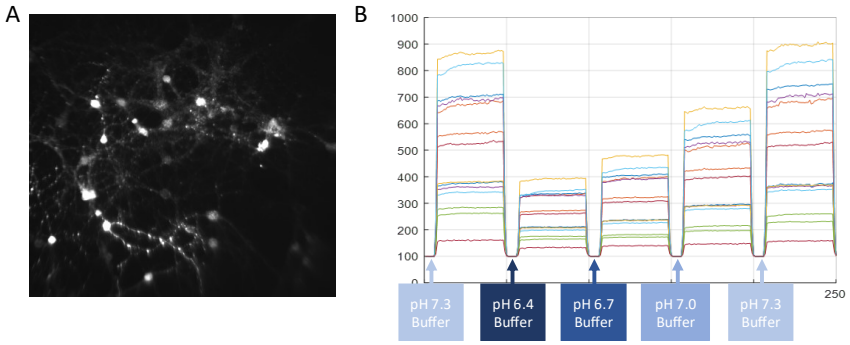

Figure 3: Procedure for calibrating pHoran4 pH measurements.

A) Representative image of cultured neurons expressing pHoran4. The cells have been permeabilized with Nigericin and are in a high K+ extracellular medium (Methods). B) Example fluorescence traces of individual cells as the dish is perfused with buffers of different pH values.

2.3.2 Acidification is via proton transport through the opsin

We next sought to determine to what extent the acidification was due to proton transport through the opsin vs through depolarization-induced opening of endogenous proton-permeable channels or other activity-dependent acidification mechanisms (e.g. metabolic shifts). Working in HEK cells, we expressed CheRiff, pHoran4 and a doxycycline-inducible inward rectifying potassium channel, $K_{ir}2.1$, (Methods, Figure 4A). The $K_{ir}2.1$ channel polarized the HEK cells to a resting potential of approximately -70 mV,[101] providing a driving force for proton entry. When the cells were grown into a confluent monolayer, they coupled electrically via endogenous gap junctions (Figure 4B).[102]

We characterized these cultures using a wide-area “Firefly” microscope which provided spatially and temporally patterned illumination at 470 and 561 nm via a digital micromirror device (DMD).[103] Figure 4C shows the protocol for interleaved CheRiff stimulation and pH imaging. After 60 s of stimulation, cells expressing all three components were acidified to a pH of 6.96 ± 0.15 (mean ± S.D., *n* = 75 cells). Cells not expressing K_{ir}2.1 had substantially less acidification (final pH 7.21 ± 0.05, mean ± S.D., *n* = 70 cells, *p* = 2e-24, Wilcoxon signed-rank test), confirming the importance of membrane voltage as a driving force for proton entry. Cells lacking both the CheRiff and the K_{ir}2.1 did not show detectable acidification (final pH 7.31 ± 0.02, mean ± S.D., *n* = 13 cells, Figure 4D-F), consistent with our results in neurons (Figure 2E, F).

These results established that acidification occurred in non-excitable cells but left open the possibility that the HEK cells might contain an endogenous proton conductance that opened upon membrane depolarization. To test this possibility, we took advantage of the gap junctional coupling between cells in a confluent monolayer. Due to the gap junctions, local CheRiff activation led to depolarization of neighboring regions, with an electrotonic length constant of ~300 μm.[102] While protons can also diffuse through gap junctions, this process is orders of magnitude slower than propagation of membrane voltage.[104] This difference in lateral electrical vs proton transport permitted us to indirectly depolarize cells via gap junction coupling, and to ask whether the acidification arose in all depolarized cells or only in cells with direct CheRiff activation.

We used the DMD to pattern the optogenetic stimulation into stripes, with a separation between the stripes of 95 μm, much smaller than the electrotonic length constant (Figure 4G). We used the far-red voltage sensitive dye BeRST1[105] to map the voltage changes throughout the sample. Figure 4H shows the stimulus pattern (reported via fluorescence of CheRiff-GFP), and the electrical depolarization pattern. As expected from the strong gap junctional coupling, the optogenetically induced depolarization in the interstitial “Blue Off” regions was almost as large as in the directly stimulated “Blue On” regions (Figure 4I).

We then mapped the pH changes over the whole field of view, using the same striped stimulation pattern alternating with wide-field yellow illumination for pH imaging (Figure 4J). In the directly stimulated “Blue

On" regions we observed robust acidification after 13.5 s (pH = 7.27 ± 0.016, mean ± S.D., *n* = 26 cells), and in the indirectly depolarized "Blue Off" regions we observed no acidification (pH = 7.31 ± 0.003, mean ± S.D., *n* = 19 cells, *p* = 1.5e-8 Wilcoxon signed-rank test, Figure 4K-M). These results establish that CheRiff directly acidifies polarized cells via proton transport through the opsin, and that electrical depolarization alone is insufficient to drive acidification.

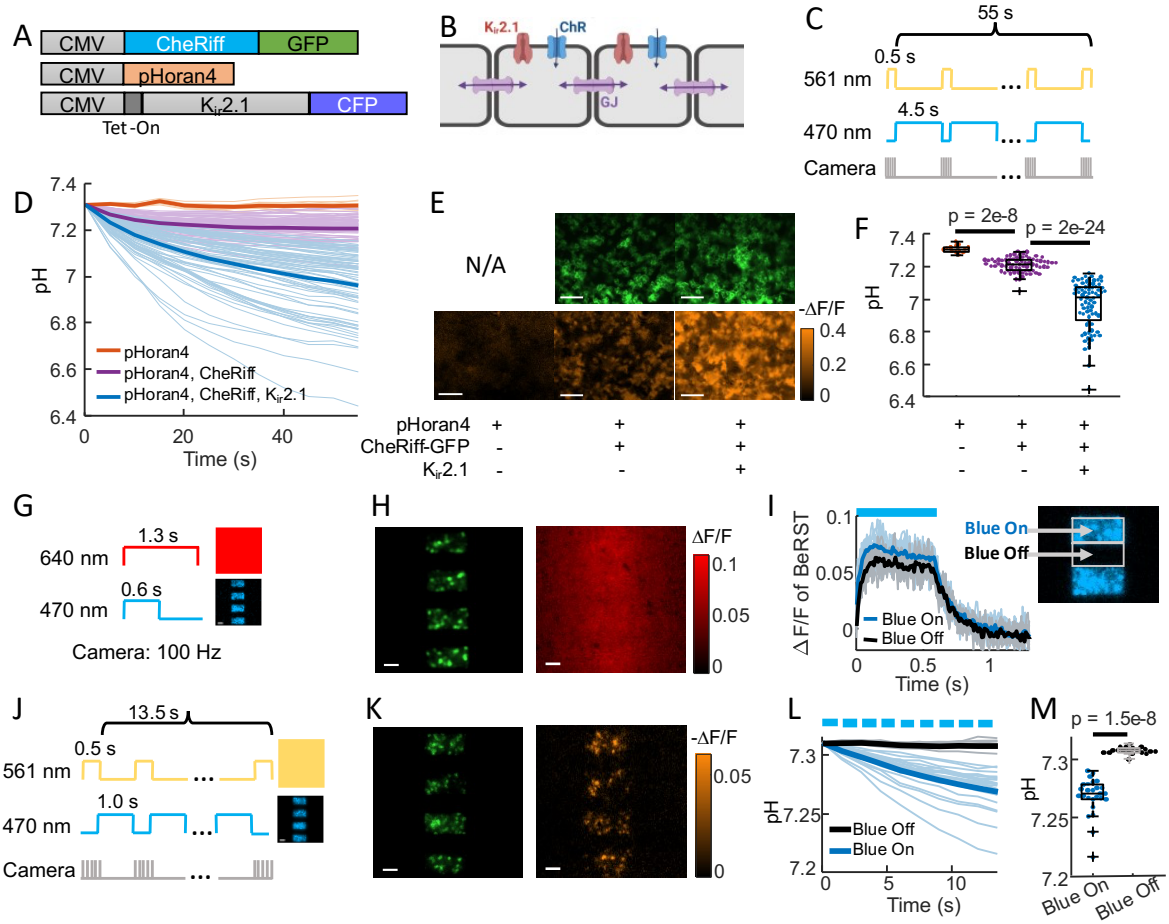

Figure 4: CheRiff exhibits high proton conductance.

A) Genetic constructs for simultaneous optogenetic stimulation and pH imaging in polarized HEK293T cells. B) Diagram of HEK cell monolayer connected by gap junctions. C) Experimental paradigm for measuring pH responses to optogenetic stimulation. Stimulation (488 nm) and measurement (561 nm) were interleaved to avoid optical crosstalk. D) Time-course of pH in HEK cells. Expression of Kir2.1 increased the driving force for proton influx, substantially enhancing the acidification. E) Images of HEK cell monolayers showing (top) GFP fluorescence, a marker for CheRiff expression and (bottom) -ΔF/F in the pHoran4 channel after protocol shown in (C). Scale bars 100 μm. F) Quantification of the data in (D-

E). pHoran4 alone: pH = 7.31 ± 0.02 (mean ± S.D., n = 13 cells); CheRiff and pHoran4 pH = 7.21 ± 0.05 (n = 70 cells); CheRiff, pHoran4 and Kir2.1: pH = 6.96 ± 0.15 (n = 75 cells). Statistical comparisons via Wilcoxon signed rank test. G) Protocol for mapping voltage responses to patterned optogenetic stimulation (488 nm) via fluorescence of BeRST1 (640 nm exc.). H) Images of HEK cell monolayers showing (left) fluorescence of GFP with patterned blue illumination, (right) ΔF/F of BeRST1. Scale bars 100 μm. I) Time-course of BeRST1 fluorescence in HEK cells inside (Blue On) and outside (Blue Off) the optogenetic stimulus regions. J) Protocol for measuring pH responses to patterned optogenetic stimulation. Stimulation (488 nm) and measurement (561 nm) were interleaved to avoid optical crosstalk. K) (Left) Fluorescence of GFP with patterned blue illumination, (right) ΔF/F in the pHoran4 channel after protocol shown in (J). Scale bars 100 μm. L) Time-course of pH inside (Blue On) and outside (Blue Off) the optogenetic stimulus regions. M) Quantification of the data in (L). Directly stimulated cells acidified to pH = 7.27 ± 0.016 (mean ± S.D., n = 26 cells), indirectly depolarized cells (Blue Off) did not acidify: pH = 7.31 ± 0.003 (n = 19 cells, p = 1.5e-8 Wilcoxon signed-rank test).

2.3.3 ChR2-3M and PsCatCh2.0 are potent non-acidifying channelrhodopsins

Several channelrhodopsins were recently reported to have low proton conductivity,[99,106–109] so we tested two of these for acidification in HEK cells and characterized their photophysical properties. PsCatCh2.0[99] is derived from the highly blue shifted *Platymonas subcordiformis* PsChR[110] via the L115C mutation and addition of a trafficking signal, ER export signal, and cleavable N-terminal Lucy-Rho signal peptide. Due to its high speed and high light sensitivity, this opsin has been used for visual function restoration in blind mice.[99]

The second opsin we tested is derived from the recently engineered ChR2-XXM (i.e. ChR2-D156H), which shows high photocurrent and high selectivity for Na^+ and K^+ over H^+.[106,109] Mutating H134 to Q at the intracellular gate further enhanced the Na^+ and K^+ selectivity and photocurrent amplitude. Mutating E101 to N near the extracellular gate site also boosted the Na^+ and K^+ selectivity without affecting the photocurrent amplitude. To optimize expression and trafficking, we added the same trafficking, ER export, and signal peptides as in PsCatCh2.0. We designate this triple mutant of ChR2 as “ChR2-3M”.

Following the same procedure as in Figure 4C, we tested the acidification due to opsin stimulation in electrically polarized HEK cells expressing pHoran4, $K_{ir}2.1$, and either CheRiff, ChR2-3M, or PsCatCh2.0 (Figure 5A). After a 55 s stimulation and imaging protocol, CheRiff cells showed a decrease in pH as above (pH = 6.98 ± 0.15, mean ± S.D., n = 170 cells), while the new opsins did not show any significant changes in pH (ChR2-3M: pH = 7.31 ± 0.10, n = 63 cells; PsCatCh2.0: pH = 7.30 ± 0.03, n = 74 cells; p = 4e-31, p = 4e-35, Wilcoxon signed-rank test; Figure 5B-D). These experiments confirmed the low proton

permeability of ChR2-3M and PsCatCh2.0. In paired experiments, we used voltage imaging with BeRST1 to confirm that all three opsins induced depolarization in the HEK cell monolayers (Figure 6).

We then performed a detailed characterization of the new opsins using patch clamp electrophysiology in HEK cells (Figure 5E-I,

	Reversal Potential (mV)	ton fastest (ms)	ton at EPD50 (ms)	toff (ms)	EPD50 (mW cm-2)	Steady state photocurrent (pA)	Ipeak/ISS
CheRiff	4	4.5 ± 0.3	-	16 ± 0.8	22 ± 4	1,300 ± 80	0.65
ChR2-3M (n=4)	16.6 ± 3.6	57 ± 21	800 ± 550	1,950 ± 500	11.6 ± 8.7	1,378 ± 618	1
PsCatCh 2.0 (n=6)	12.3 ± 4.7	4.2 ± 3.5	9.3 ± 1.2	17.6 ± 3.4	116 ± 13	847 ± 359	0.92

Table 1). Both opsins were sensitive to blue (488 nm) light. ChR2-3M passed unusually large steady-state photocurrents (1378 ± 618 pA, mean ± S.D., n = 4 cells) and was highly sensitive to blue light (EPD50 = 11.6 ± 8.7 mW cm^{-2}, Figure 5E), but had slow opening (τ_{on} = 57 ± 21 ms at saturating blue light) and very slow closing (τ_{off} = 1950 ± 500 ms, Figure 5F). PsCatCh2.0 had somewhat smaller photocurrents (847 ± 359 pA, *n* = 6 cells), higher EPD50 (116 ± 13 mW cm^{-2}), but very fast opening (τ_{on} = 4.2 ± 3.5 ms at saturating blue light) and closing (τ_{off} = 17.6 ± 3.4 ms).

Both opsins had positive reversal potentials (ChR2-3M: 16.6 ± 3.6 mV, PsCatCh2.0: 12.3 ± 4.7 mV), consistent with preferential Na^+ and Ca^{2+} selectivity (Figure 5G). A key attraction of PsCatCh2.0 for quantitative optogenetics experiments was its very flat-top response to a step in blue light. In contrast to CheRiff, which shows substantial sag in photocurrent upon continuous illumination,[100] PsCatCh2.0 showed almost no sag.

For applications in all-optical electrophysiology (i.e. simultaneous stimulation and voltage or calcium imaging), it is critical that the light used for imaging a red-shifted reporter does not interfere with the action of the opsin. At 50 mW cm^{-2} excitation intensity, ChR2-3M retained substantial activation at 561 nm (20%) and 594 nm (4.8%), but undetectable activation at 640 nm (< 0.3%, Figure 5H). PsCatCh2.0 was

more promising for all-optical applications: at 561 nm the photocurrent was only 2% and at 594 and 640 nm the photocurrent was undetectable (< 0.3%).

In some opsins, light at a red-shifted wavelength can reverse retinal isomerization, forcing the channel closed.[111,112] To mimic the conditions of a typical all-optical electrophysiology experiment, we thus tested the combination of blue (240 mW cm^{-2}) and intense orange (594 nm, 1 W cm^{-2}) or red (640 nm, 8 W cm^{-2}) light (Figure 5I). The orange light had negligible activating or inactivating crosstalk into PsCatCh2.0 activation, but partially activated the ChR2-3M (~20%). The red light slightly activated both constructs (~10% for ChR2-3M and ~5% for PsCatCh2.0), and also substantially inactivated ChR2-3M, leading to a ~40% drop in photocurrent. Together, these results indicate that PsCatCh2.0 is a particularly promising channelrhodopsin for all-optical physiology experiments.

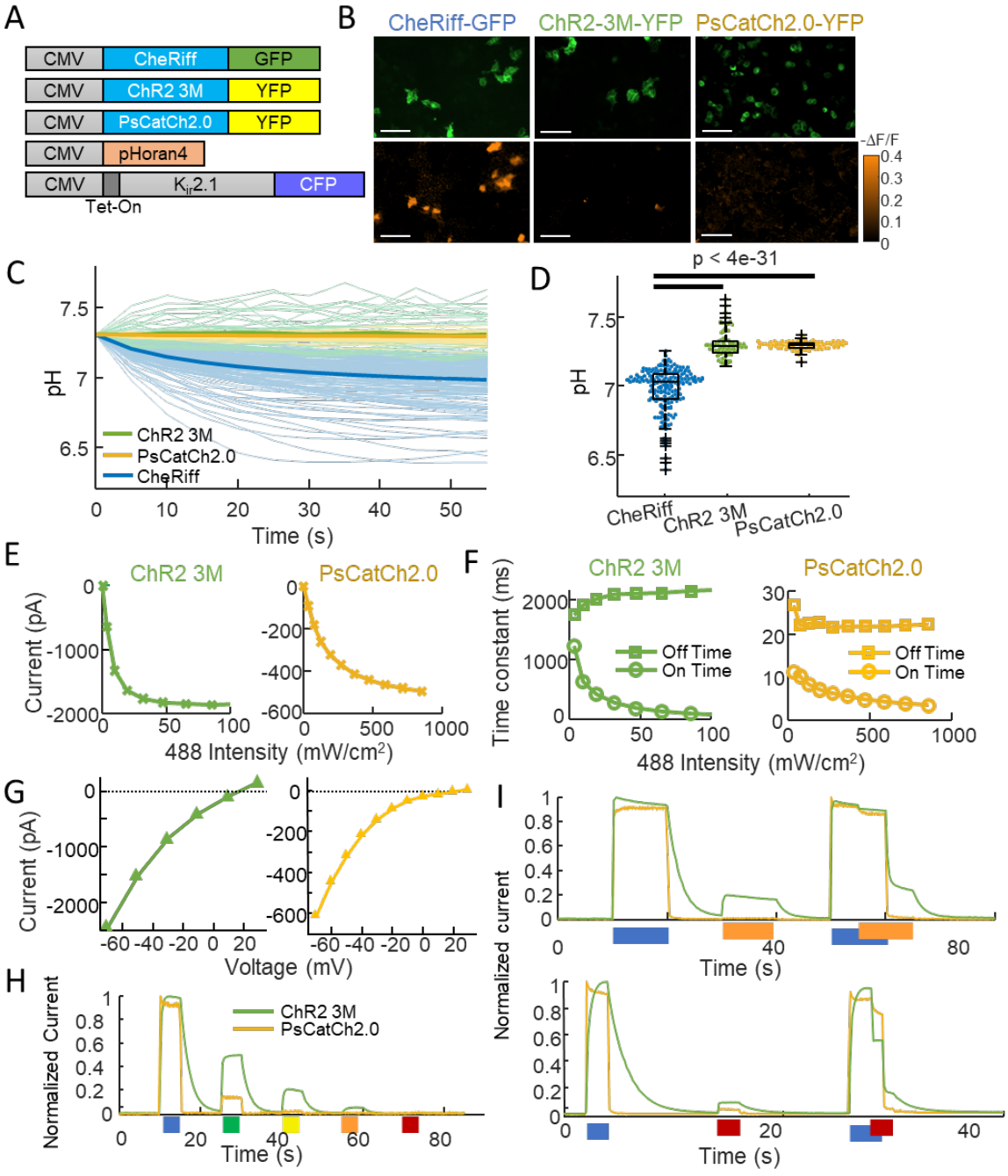

Figure 5: ChR2-3M and PsCatCh2.0 are potent non-acidifying channelrhodopsins.

A) Genetic constructs for simultaneous optogenetic stimulation using channelrhodopsin variants and pH imaging in polarized HEK cells. B) Images of HEK cells showing (top) GFP or YFP fluorescence, a marker for channelrhodopsin expression and (bottom) -ΔF/F in the pHoran4 channel, measured after protocol shown in (2C). Scale bars 100 μm. C) Time-course of pH in HEK cells expressing the three opsins. D) Quantification of the data in (C). CheRiff: pH = 6.98 ± 0.15 (mean ± S.D., n = 170 cells); ChR2-3M: pH = 7.31 ± 0.10 (n = 63 cells); PsCatCh2.0: pH = 7.30 ± 0.03 (n = 74 cells); p = 4e-31, p = 4e-35, Wilcoxon signed-rank test. E-I) Whole-cell voltage clamp measurements on HEK cells expressing channelrhodopsins. E) Steady-state photocurrents as a function of blue illumination intensity. F) Opening

and closing kinetics as a function of blue light intensity. G) Steady-state photocurrents as a function of holding voltage. H) Normalized photocurrents from stimulation with light at 488 nm, 532 nm, 561 nm, 594 nm, and 640 nm (50 mW cm^{-2} in all cases). I) Normalized photocurrents from combinations of blue (488 nm, 240 mW cm^{-2}) and orange (594 nm, 1 W cm^{-2}) or red (640 nm, 8 W cm^{-2}) light corresponding to intensities typical for all-optical electrophysiology.

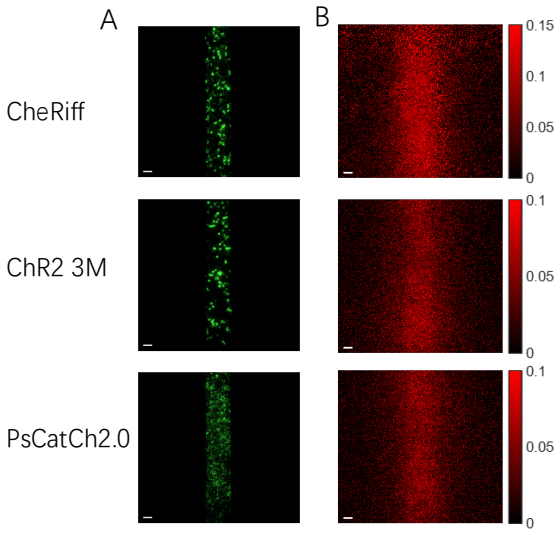

Figure 6: Depolarization of HEK cell monolayers with patterned stimulation of channelrhodopsins.

(A) GFP or YFP expression showing opsin expression in patterned stimulation region of gap junction coupled monolayer. (B) BeRST ΔF/F of Hek cell monolayer showing depolarization from patterned stimulation.

	Reversal Potential (mV)	**t_{on} fastest (ms)**	**t_{on} at EPD50 (ms)**	**t_{off} (ms)**	**EPD50 (mW cm^{-2})**	**Steady state photocurrent (pA)**	**I_{peak}/I_{ss}**
CheRiff	4	4.5 ± 0.3	-	16 ± 0.8	22 ± 4	1,300 ± 80	0.65
ChR2-3M (n=4)	16.6 ± 3.6	57 ± 21	800 ± 550	1,950 ± 500	11.6 ± 8.7	1,378 ± 618	1
PsCatCh 2.0 (n=6)	12.3 ± 4.7	4.2 ± 3.5	9.3 ± 1.2	17.6 ± 3.4	116 ± 13	847 ± 359	0.92

Table 1: Comparison of channelrhodopsin gating properties.

EPD50 is the effective power density for 50% activation. CheRiff data are from Ref.[67] Fig. S9 and Table S4. CheRiff reversal potential is from Ref.[113]

We then tested the new opsins in cultured rat hippocampal neurons (Figure 7). Under paired optogenetic stimulation and pH imaging (Figure 7A,B), we observed acidification in cells expressing CheRiff (pH = 6.87 ± 0.27, mean ± S.D., *n* = 24 cells), as before. We observed substantially less acidification in cells expressing either ChR2-3M (pH = 7.13 ± 0.19, mean ± S.D., *n* = 31 cells, *p* = 2.5e-4), or PsCatCh (pH = 7.14 ± 0.11, mean ± S.D., *n* = 25 cells, *p* = 4e-5, Figure 7C-E). We then produced cultures co-expressing each of the three channelrhodopsins and QuasAr6a for voltage imaging (Figure 7F,G). Under blue light stimulation, each opsin induced reliable spiking (Figure 7H). ChR2-3M also induced some firing in intervals after a blue light pulse, presumably due to the very slow closing of the channel leading to residual currents.

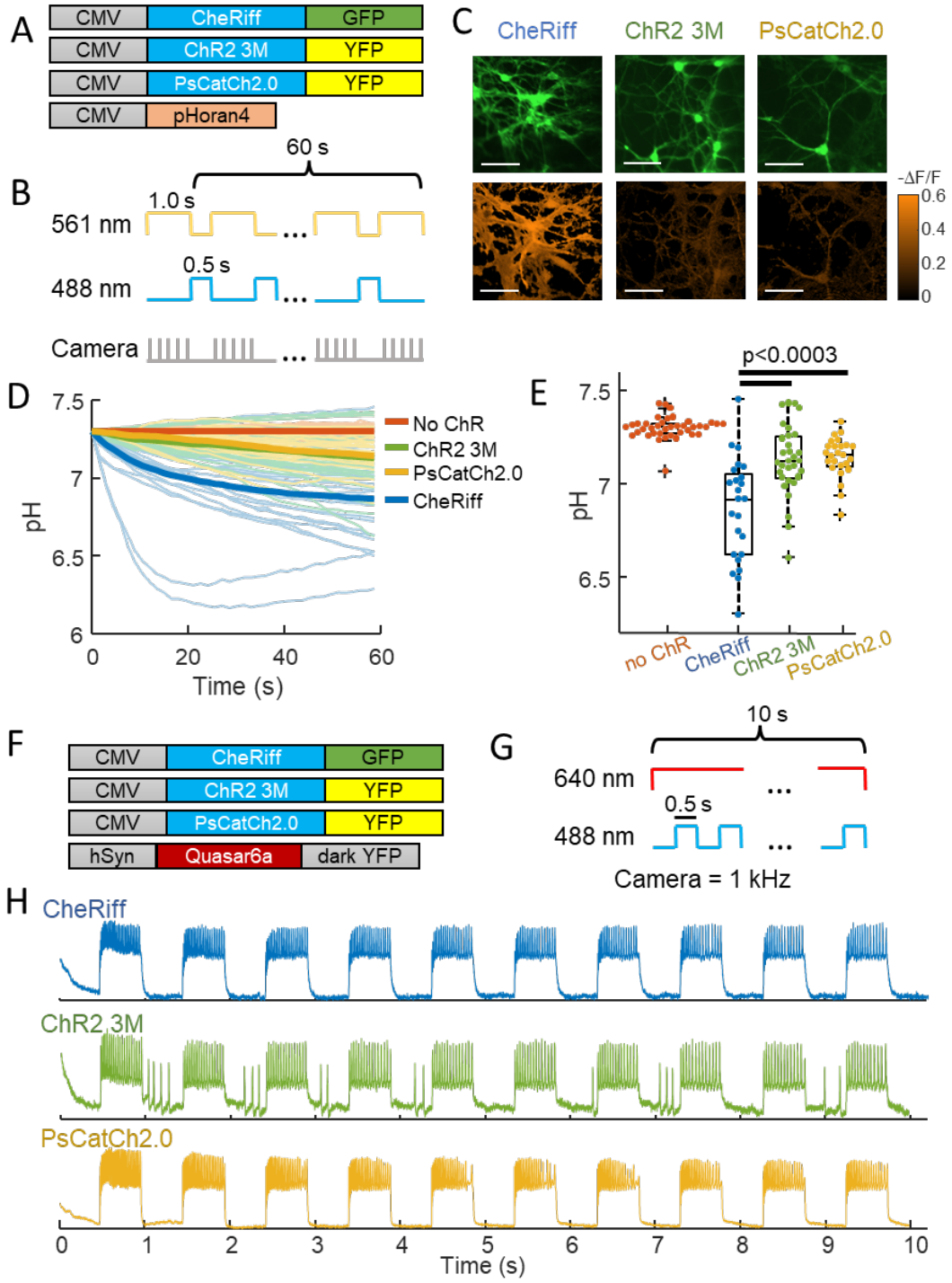

Figure 7: Chr2-3M and PsCatCh2.0 acidify neurons less than CheRiff.

A) Genetic constructs for simultaneous optogenetic stimulation and pH imaging. B) Experimental paradigm for measuring pH responses to optogenetic stimulation. Stimulation (blue) and measurement (yellow) are interleaved for 60 s to avoid optical crosstalk. C) Images of cultured neurons showing (top) GFP or YFP fluorescence, a marker for Channelrhodopsin expression, (bottom) ΔF/F in the pHoran4 channel after the protocol shown in (B). (left) CheRiff-GFP, (middle) ChR2-3M-YFP, (right) PsCatCh2.0.

Scale bars 100 μm. D) Time-course of pH dynamics in cultured neurons. Cells expressing ChR2-3M and PsCatCh2.0 acidify less than CheRiff. E) Neurons expressing ChR2-3M, pH = 7.13 ± 0.19 (mean ± S.D., n = 31 cells), and PsCatCh2.0, pH = 7.14 ± 0.11 (mean ± S.D., n = 25 cells) had significantly less acidification (p = 2.5e-4, p = 4e-5, respectively, Wilcoxon signed-rank test) than CheRiff-expressing neurons, pH of 6.87 ± 0.27 (mean ± S.D., n = 24 cells). F) Genetic constructs for simultaneous optogenetic stimulation and Voltage imaging. G) Experimental paradigm for measuring voltage responses to optogenetic stimulation. Stimulation (blue) and measurement (red). H) Time-course of optogenetically activated spiking in cultured neuron expressing (top) CheRiff, (middle) ChR2-3M, or (bottom) PsCatCh2.0.

2.4 Discussion

Most polarized cells have a strong inward-directed proton-motive force, and sodium-proton exchangers are required to maintain physiological intracellular pH.[114,115] A sudden change in proton permeability of the membrane can disrupt this balance, leading to intracellular acidification. We note that the proton flux was sufficient to overwhelm the buffering capacity of the cytoplasm. While we focused on the acidification due to CheRiff, we expect similar levels of acidification from other channelrhodopsins, unless they have been engineered specifically to be proton-impermeable.

The degree of acidification depends on the sub-cellular opsin distribution and the cell geometry. In general, the smaller the compartment, the larger the acidification. While we could not resolve individual dendritic spines, our results suggest that if channerhodopsins exist in spines, optogenetic acidification in spines could be substantial. In some all-optical physiology experiments, channelrhodopsins are restricted to the soma and proximal dendrites via trafficking sequences such as the $K_v2.1$ trafficking motif.[68] While this restriction has been primarily to facilitate targeted single-cell activation, a possible side effect is to decrease acidification in small distal compartments (dendrites, spines, axon).

Here we showed that the high-performance opsins ChR2-3M and PsCatCh2.0 have very low proton permeability, enabling repeated stimulation with minimal local acidification. We observed no activation-induced acidification in HEK cells (Figure 5C,D), but we did observe a very slight acidification in neurons (Figure 7D,E). We speculate that the activity-induced neuronal acidification was due to cell autonomous mechanism [116–118] as opposed to proton transport through the opsins.

While the ChR2-3M construct is not optimal for all-optical physiology experiments due to crosstalk with longer wavelength light, several features make it promising for prospective therapeutic applications. It

has a very high photocurrent and high sensitivity, meaning that substantial modulation can be achieved with light at intensities < 10 mW/cm^2. The slow closing of this construct could enable tonic activation with pulsed light, further decreasing the optical dose into the tissue. The positive reversal potential (+16.6 mV) further contributes to the ability of this channelrhodopsin to depolarize cells, even when the cells are already partially depolarized. Together with its low proton permeability, these attributes make ChR2-3M a good candidate for therapeutic applications requiring slowly varying changes in optogenetic drive.

2.5 Materials and Methods

HEK293T cell culture: Wild-type or engineered HEK293T cell lines were maintained at 37 °C, 5% CO_2 in Dulbecco's Modified Eagle Medium (DMEM) supplemented with 10% fetal bovine serum, 1% GlutaMax-I, penicillin (100 U/mL), streptomycin (100 μg/mL). For maintaining or expanding the cell culture, we used TC-treated culture dishes (Corning). For all imaging experiments, cells were plated on PDL-coated glass-bottomed dishes (Cellvis, Cat.# D35-14-1.5-N).

Neuron culture: Primary E18 rat hippocampal neurons (fresh, never frozen, BrainBits #SDEHP) were dissociated following vendor protocols and plated in PDL-coated glass bottom dishes (Cellvis, Cat.# D35-14-1.5-N). Neurons (21k/cm^2) were cocultured with primary rat glia (27k/cm^2) to improve cell health and maturation.

Lentivirus preparation: All the lentivirus preparations were made in house. HEK293T cells were co-transfected with the second-generation packaging plasmid psPAX2 (Addgene #12260), envelope plasmid VSV-G (Addgene #12259) and transfer plasmids at a ratio of 9:4:14. For small batches, 2.7 μg total plasmids for a small culture (300k cells in 35-mm dish) gave sufficient yield of lentivirus. Some viruses were concentrated using Lenti-X Concentrator (Takara Cat. # 631232) following vendor protocols and were concentrated 1/10. Quantities of virus used were quoted as non-concentrated amounts.

Expression of optogenetic actuators and reporters:

HEK293T cells were transduced at least 2 days before imaging with 50-200 μL of lentivirus encoding the desired Channelrhodopsin. Cell lines were created for stable expression of pHoran4, and of pHoran4 with

Dox inducible K_{ir}2.1-CFP, using fluorescence activated cell sorting (FACS) on cells that already had stable rtTA3 expression through antibiotic selection. K_{ir}2.1 expression was induced 2 days before imaging by adding 1 μg/mL doxycycline, which was kept on the culture until time to image.

Neurons were transduced after 6-10 days in culture with 1) 200 μL lentivirus encoding pHoran4 driven by the CMV promoter, or 100-200 μL lentivirus encoding Quasar6a driven by the synapsin promoter and 2) 50-200 μL of the Channelrhodopsin variants, also driven by the CMV promoter. Functional imaging was performed after 14-20 days in culture.

pH calibration: The pH response of pHoran4 was calibrated by changing the buffer pH stepwise from 6.4 to 7.3 (Figure S1). To equilibrate the pH of the cytosol with the buffer pH, we added the K^+/H^+ exchanger nigericin at 14 μM. To prevent a $[K^+]$ gradient from driving a proton gradient, we used a high-potassium extracellular buffer ([119],[120]). The buffer composition was (in mM): Good's zwitterionic buffer 25, KCl 100, NaCl 38, $CaCl_2$ 1.8, $MgSO_4$ 0.8, NaH_2PO_4 0.9. The Good buffer, chosen based on its pK_a and effective buffering pH range, was MES for pH 6.4 and HEPES for pH 6.7–7.3. After perfusion of the buffers with different pH values, we waited 1 minute for the pH to equilibrate and recorded the steady state fluorescence for each cell. $\Delta F/F$ was calculated using the pH 7.3 as the baseline. The $\Delta F/F$ at each pH was then averaged across cells, and this average was fit with piecewise linear interpolation, which was used for converting $\Delta F/F$ to pH in subsequent data analysis.

Sample preparation for imaging: Before optical stimulation and imaging, 35 mm dishes were washed with 1 mL PBS to remove residual culture medium, then filled with 2 mL extracellular (XC) buffer containing (in mM): 125 NaCl, 2.5 KCl, 2 $CaCl_2$, 1 $MgCl_2$, 15 HEPES, 25 glucose (pH 7.3). All imaging and electrophysiology were done using this XC buffer. For voltage imaging experiments in neurons, we added 10 μM NBQX, 20 μM Gabazine, 25 μM AP-V to block synaptic transmission.

BeRST1 was a gift from Evan Miller (Berkeley) and was used for voltage imaging in HEK cell monolayers. Cells were washed to remove culture medium and then incubated with 1-2 μM BeRST1 dye in XC buffer for 30 minutes. Immediately before imaging, samples were washed twice and immersed in XC buffer.

Combined optogenetic stimulation and imaging: Experiments were conducted on a home-built inverted fluorescence microscope equipped with 405 nm, 488 nm, 532 nm, 561 nm, 594 nm, and 640 nm laser lines and a scientific complementary metal-oxide semiconductor (CMOS) camera (Hamamatsu ORCA-Flash 4.0). Beams from lasers were combined using dichroic mirrors and sent through an acousto-optic tunable filter (Gooch and Housego TF525-250-6-3-GH18A) for temporal modulation of intensity of each wavelength. The beams were then expanded and sent either to a DMD (Vialux, V-7000 UV, 9515) for spatial modulation or sent directly into the microscope (to avoid power losses associated with the DMD). The beams were focused onto the back-focal plane of a 60×/1.2-NA (numerical aperture) water-immersion objective (Olympus UIS2 UPlanSApo ×60/1.20W) or a 20×/0.75-NA objective (Olympus UIS2 UPlanSApo ×20/0.75). For Green and Yellow fluorescent protein, pHoran4, and QuasAr6a, fluorescence emission was separated from laser excitation using a dichroic mirror (488/561/633). Imaging of pHoran4 fluorescence was performed with 561 nm laser at illumination intensities of 100-200 mW cm^{-2}. Imaging of QuasAr6a fluorescence was performed with 640 nm laser at an illumination intensity of 8 W cm^{-2}. Stimulation of Channelrhodopsins was performed with 488 nm laser at an illumination intensity of 400–800 mW cm^{-2}.

Electrophysiology: For patch clamp measurements, filamented glass micropipettes (WPI) were pulled to a resistance of 5–10 MΩ and filled with internal solution containing (in mM) 6 NaCl, 130 K-aspartate, 2 $MgCl_2$, 5 $CaCl_2$, 11 EGTA, and 10 HEPES (pH 7.2). The patch electrode was controlled with a low-noise patch clamp amplifier (either A-M Systems model 2400 or Axon Instruments MultiClamp 700B). Current traces were collected in voltage clamp mode. The collected electrophysiology data had a moving average filter applied to help reduce noise. The time constants were fit using single exponentials. In plots with multiple wavelengths of stimulation, the currents were normalized to the peak current for 488 nm stimulation.

Wide-field imaging and patterning: Spatially resolved optical electrophysiology measurements were performed using a home-built upright ultra-wide-field microscope[121] with a large field of view (4.6 × 4.6 mm^2, with 2.25 × 2.25 μm^2 pixel size in the sample plane) and high numerical aperture objective lens (Olympus MVPLAPO 2XC, NA 0.5). The fluorescence of BeRST1 was excited with a 639 nm laser

(OptoEngine MLL-FN-639) at 100 mW cm^{-2}, illuminating the sample from below at an oblique angle to minimize background autofluorescence. BeRST1 fluorescence was separated from scattered laser excitation via a dichroic beam splitter (Semrock Di01- R405/488/561/635-t3–60x85) and an emission filter (Semrock FF01-708/75–60-D). Images were collected at a 100 Hz frame rate on a Hamamatsu Orca Flash 4.2 scientific CMOS camera. Optogenetic stimulation was performed by exciting Channelrhodopsins with a blue LED (Thorlabs M470L3) with a maximum intensity of 400 mW cm^{-2}.

Measuring permeability of ChR2-3M: *Xenopus* oocytes were injected with cRNAs and maintained at 16 °C for 2 days in ND96 solution: 96 mM NaCl, 2 mM KCl, 1 mM $CaCl_2$, 1 mM $MgCl_2$, 10 mM HEPES, pH 7.4, and 50 µg/mL gentamycin. Two-electrode voltage-clamp was used for oocyte electrophysiology with TURBO TEC-05 amplifier from NPI (NPI electronics GmbH, Tamm, Germany). For current amplitude comparisons, photocurrents were measured in extracellular solution containing 110 mM NaCl, 5 mM KCl, 2 mM $MgCl_2$, 2 mM $BaCl_2$, 5 mM HEPES, pH 7.6; holding at -70 mV. Shifts in reversal potential, V_r, were calculated by the reversal potential differences upon changing extracellular Na^+ or K^+ concentration from 120 mM (120 mM NaCl/KCl, 2 mM $BaCl_2$, 5 mM HEPES, pH adjusted to 7.6 by N-Methyl-D-glucamine) to 1 mM (1 mM NaCl/KCl, 119 mM N-Methyl-D-glucamine, 2 mM $BaCl_2$, 5 mM HEPES, pH adjusted to 7.6 by HCl). For all oocyte experiments, 473 nm laser at 5 mW/mm^2 was used for illumination.

Data Analysis: All data were processed and analyzed in MATLAB. For recordings with interleaved optogenetic stimulation and pH imaging, camera frames during stimulation were discarded, and frames during each period of imaging were averaged. Baseline fluorescence, F_0, was calculated from the first frame, before any optogenetic stimulation. A threshold on F_0 was set to restrict calculation of $\Delta F/F_0$ to signal-bearing regions of the sample.

Individual cells expressing the desired constructs were selected and fluorescence waveforms were calculated by averaging pixels whose baseline value exceeded the threshold. Sensor photoactivation artifacts were characterized using matched controls that expressed pHoran4 but no channelrhodopsin. Population-average photoartifacts were subtracted from the signals obtained from cells with channerhodopsin expression.

Dendrites were selected and analyzed in the same manner as somas, and were then associated with the connected soma. Acidification half-times were calculated by finding the maximum acidification during the stimulation period, and then finding the time point where the $\Delta F/F$ first reached half of the maximum decrease. Recovery after stimulation was fit to a single exponential, and the fit function was used to calculate the half-recovery time. Statistical tests are done using the Wilcoxon signed-rank test.

Chapter 3 All-optical mapping of Ca^{2+} transport and homeostasis in dendrites

3.1 Abstract

Calcium mediates many important signals in dendrites. However, the basic transport properties of calcium in dendrites have been difficult to measure: how far and how fast does a local influx of calcium propagate? We developed an all-optical system for simultaneous targeted Ca^{2+} import and concentration mapping. We co-expressed a blue light-activated calcium selective channelrhodopsin, CapChR2, with a far-red calcium sensor, FR-GECO1c, in cultured rat hippocampal neurons, and used patterned optogenetic stimulation to introduce calcium into cells with user-defined patterns of space and time. We determined a mean steady-state length constant for Ca^{2+} transport ϕ ~ 5.8 μm, a half-life for return to baseline $t_{1/2}$ ~ 1.7 s, and an effective diffusion coefficient D ~ 20 $\mu m^2/s$, though there were substantial differences in Ca^{2+} dynamics between proximal and distal dendrites. At high Ca^{2+} concentration, distal dendrites showed nonlinear activation of Ca^{2+} efflux, which we pharmacologically ascribed to the NCX1 antiporter. Genetically encoded tools for all-optical study of Ca^{2+} transport and handling provide a powerful capability for studying this important messenger.

3.2 Introduction

Calcium is an important signaling molecule in all kingdoms of life.[122] In mammals, Ca^{2+} is involved in many crucial functions, such as muscle contraction,[123] hormone secretion,[124] and neural activity and plasticity.[125] The cytoplasmic Ca^{2+} concentration is determined by a complex interplay of transport across the plasma membrane, transport to and from internal stores in the endoplasmic reticulum (ER) and mitochondria, and buffering by Ca^{2+} binding proteins.

Ca^{2+} signaling is often compartmentalized to sub-cellular locations to achieve region-specific effects.[126–128] This compartmentalization can occur over nanodomains associated with individual Ca^{2+} channels,[129] microdomains associated with clusters of Ca^{2+} channels,[130] or over larger regions defined by the geometry of the cell membrane, such as within presynaptic boutons,[131] dendritic spines,[132] primary cilia,[133] or individual dendrite branches.[134,135]

To study sub-cellular Ca^{2+} transport and homeostasis, one would like to induce Ca^{2+} influx in arbitrary patterns of space and time, and to map the resulting time-dependent Ca^{2+} concentration profiles. A genetically encoded system would also permit targeting specific cell types. All-optical genetically encoded tools for targeted perturbation and measurement are a powerful approach to mapping spatiotemporal responses of cellular signals. For example, we have developed all-optical systems for perturbation and measurement of voltage,[100,136,137] of cAMP,[70] and of the embryonic morphogen Nodal.[138]

Here we co-expressed a blue-excited calcium-selective channelrhodopsin CapChR2[139] with a far-red fluorescent Ca^{2+} indicator protein FR-GECO1c[34] in cultured rat hippocampal neurons. We used optical patterning to introduce local calcium fluxes and determined the resulting steady state length-constant for Ca^{2+} spread. We then used wide-area channelrhodopsin activation to map cell-wide Ca^{2+} recovery kinetics. We combined these measurements to infer the effective diffusion coefficient of Ca^{2+} ions in the dendrites. We then explored how blocking the sodium-calcium exchanger NCX1 affected Ca^{2+} transport and recovery after a perturbation.

3.2.1 Simple model: 1-D reaction diffusion

Reaction-diffusion dynamics provide a conceptual framework for interpreting the experiments below, so we introduce the relevant formulas and terms here. Similar ideas have been presented elsewhere, e.g. Ref. [140]. We treat each dendrite as a 1-D tube (we ignore branching). The Ca^{2+} dynamics then follow:

$$\frac{\partial C}{\partial t} = D\frac{\partial^2 C}{\partial x^2} - kC + S(x,t),$$

Equation 1

where x is the contour coordinate along the tube, C is the deviation from equilibrium Ca^{2+} concentration, D is an effective diffusion coefficient, and k is a rate constant for return of Ca^{2+} to equilibrium. $S(x,t)$ is the source density, i.e. the time-dependent injection or removal of Ca^{2+} into the dendrite, such as by CapChR2. Here D can (and does) differ substantially from the free-solution diffusion coefficient, because it includes the effects of interactions with buffers, uptake and release from internal stores, occlusion by organelles, and transient trapping of Ca^{2+} ions in dendritic spines. Here k captures the effects of all Ca^{2+} transport processes which tend to return the Ca^{2+} concentration to its equilibrium value. This includes transport across the plasma membrane, and also uptake by internal stores.

Eq. 1 is a linear partial differential equation, which can be solved by standard techniques. A sum of two solutions is also a solution. It is therefore convenient to introduce the impulse response, or Green's function, $G(x,t)$. To calculate the concentration profile for an arbitrary time-dependent input $S(x,t)$, one simply convolves $G(x,t)$ with $S(x,t)$. Under steady-state conditions, i.e. $S(x,t) = S(x)$, the steady state Green's function, $G_{ss}(x)$, is particularly simple:

$$G_{ss}(x) = \frac{1}{Dk}\exp\left(-\frac{|x|}{\phi}\right),$$

Equation 2

where the length constant $\phi = \sqrt{D/k}$. This Green's function gives the steady state calcium concentration profile around a constant Ca^{2+} flux localized around $x = 0$, i.e. for $S(x) = \delta(x)$.

For a spatially homogeneous initial deviation in concentration C_0, the time-dependent deviation in concentration is $C(t) = C_0\exp(-k\,t)$. Thus, by measuring length constant ϕ and recovery rate constant k, one can determine the effective diffusion coefficient $D = \phi^2 k$. For a more detailed discussion of Eq. 1 and its time-dependent solutions, see e.g. Ref. [70].

The above framework is an oversimplification of reality. It assumes that the underlying dynamics are linear, spatially homogeneous, and constant in time. There are many reasons to doubt these assumptions. As Ca^{2+} concentration increases, intracellular buffers become saturated and the fraction of bound vs. free Ca^{2+} changes, leading to changes in D,[141] a situation handled by nonlinear models of buffered diffusion.[142] Ca^{2+} dynamics can also be nonlinear because of Ca^{2+}-induced Ca^{2+} release or uptake by the endoplasmic reticulum[143,144] and mitochondria[145]. Finally, the inhomogeneous distribution of mitochondria can cause localized anomalies in Ca^{2+} concentrations,[135] the approximation of the dendrite as a featureless 1-D tube is clearly incorrect, and Ca^{2+} buffering and transport are subject to plasticity at multiple timescales.[146,147] Despite being an oversimplification, the model above is useful for predicting scaling properties of Ca^{2+} transport and for identifying deviations from the model assumptions.

3.3 Results

3.3.1 All-optical Ca^{2+} perturbation and measurement with genetically encoded tools

We created an all-optical system for mapping Ca^{2+} signaling by co-expressing an actuator and reporter of Ca^{2+} (Figure 8A). To introduce controlled perturbations to Ca^{2+}, we used CapChR2-eGFP[139], a Ca^{2+} selective cation channel with an activation peak at 475 nm. We first performed a detailed characterization of CapChR2 in HEK293T cells using whole-cell patch clamp electrophysiology (Figure 8B–F). CapChR2 was highly sensitive to blue light (intensity for 50% activation, I_{50} = 0.035 mW/mm^2, Figure 8C). The opening and closing time constants at 37 °C and 1.45 mW/mm^2 were τ_{on} = 19 ± 3 ms and τ_{off} = 81 ± 14 ms, (mean ± s.e.m. n = 3 cells). The kinetics were slower at lower intensity or lower temperature (Figure 8D). CapChR2 had a positive reversal potential (10 mV, Figure 8E), consistent with preferential Ca^{2+} selectivity. CapChR2 showed negligible sag in photocurrent during sustained illumination (Figure 8F).

To test whether the light used for imaging the red-shifted Ca^{2+} reporter affected the opsin, we compared CapChR2 photocurrents under blue (488 nm), orange (594 nm) and combined blue + orange illumination. At matched intensities of 0.22 mW/mm^2, the photocurrent from orange light was only 8% of the photocurrent from blue light (Figure 8F). In some opsins, red or orange light can drive a transition from

the open to the closed state.[111,148] To test for this effect, we applied blue light (488 nm, 0.22 mW/mm^2), and then after a 3.5 s delay, we applied orange light (594 nm, 0.21 mW/mm^2) while maintaining the blue illumination (Figure 8F). The orange light induced a decrease in photocurrent of ~10%. Since the orange illumination was constant and homogeneous in our measurements, this slight decrease in overall CapChR2 photocurrent was not consequential.

To map the CapChR2-evoked Ca^{2+} concentration profile, we used FR-GECO1c,[34] a far-red Ca^{2+} reporter with an excitation peak at 596 nm. This reporter has previously been characterized in detail. The reported response properties relevant to our study are: calcium affinity 83 nM, maximum response amplitude ($\Delta F/F$) 18, Hill coefficient 2, rise half-time 13 ms, decay half-time 156 ms.[34]

We then tested the combined system in cultured neurons. Cultured neurons were transduced with separate lentiviral vectors for FR-GECO1c and CapChR2-eGFP. We used a custom microscope (Methods, Figure 8G) in which 594 nm light and 488 nm light were combined, passed through an acousto-optical tunable filter, and patterned via a digital micromirror device (DMD, Figure 8G) which was re-imaged onto the sample. By rapidly alternating between orange and blue illumination and synchronously switching between two DMD patterns, we could create arbitrary and independent spatial patterns of orange and blue illumination. Provided that the alternation was faster than the biological response times of the sample, the flicker had negligible effect.

All experiments were performed in 2 μM TTX to block spiking, so that changes in intracellular Ca^{2+} were primarily mediated by CapChR2 currents. Two-color imaging under wide-field 488 nm and 594 nm illumination identified cells which co-expressed the actuator and reporter (Figure 8H). These cells showed a large increase of the FR-GECO1c signal in the soma during wide-area blue light stimulation, ($\Delta F/F$ = 0.77 ± 0.50, mean ± s.d., n = 9 neurons). In neurons expressing only FR-GECO1c the fluorescence change was much smaller ($\Delta F/F$ = 0.026 ± 0.014, mean ± s.d., n = 7 neurons, Figure 8I, J). These experiments established that optical stimulation of CapChR2 caused Ca^{2+} influx to the cytosol and a corresponding increase in FR-GECO1c fluorescence, while blue light stimulation evoked negligible optical crosstalk in FR-GECO1c alone.

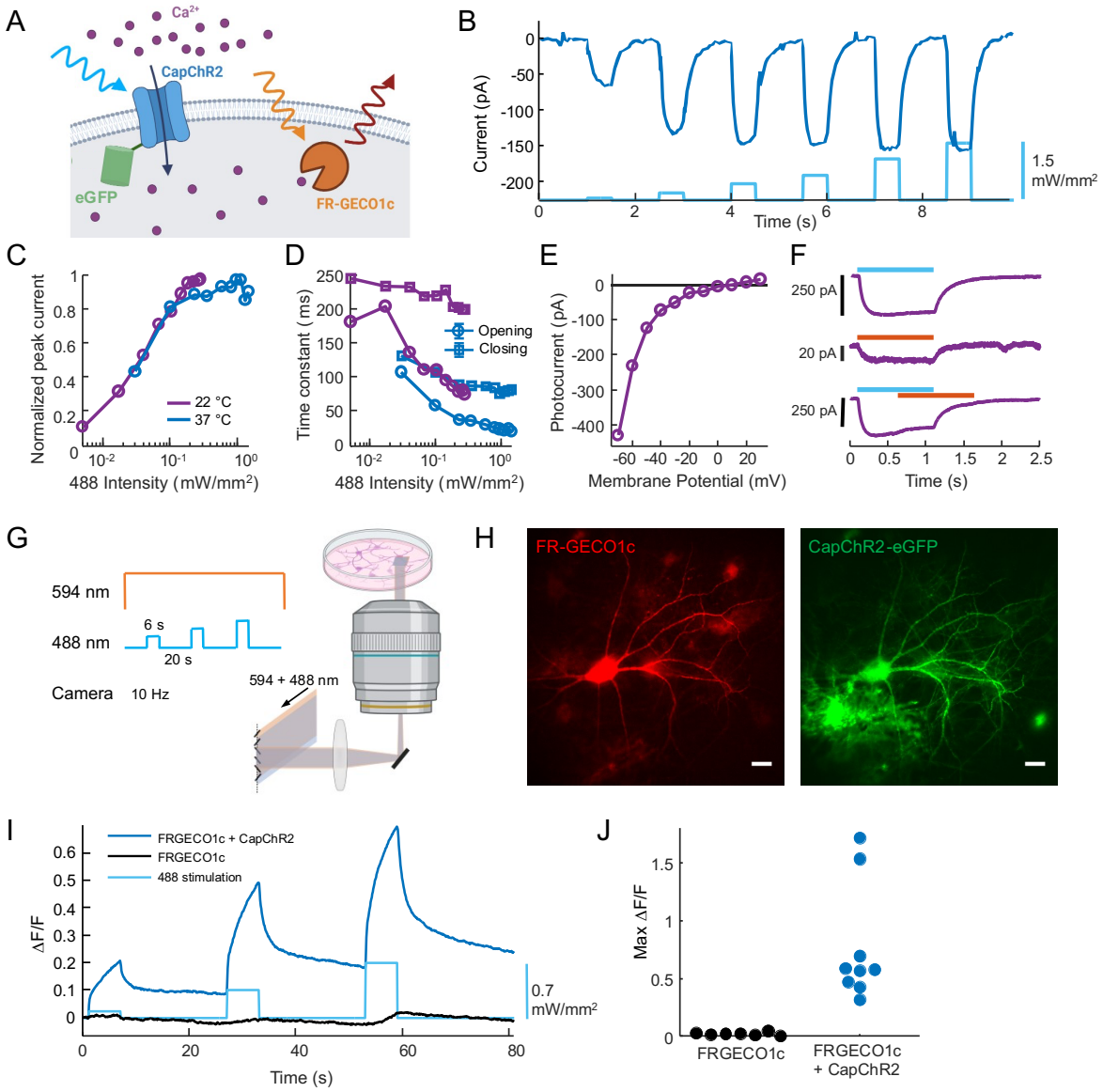

Figure 8: All-optical perturbation and measurement of Ca2+ dynamics.

A) A blue light-activated Ca2+-selective Channelrhodopsin, CapChR2 is co-expressed with an orange-light excited Ca^{2+} sensor, FR-GECO1c. B) Example recording of CapChR2 photocurrents in a HEK293T cell at 37 ºC. Holding voltage -70 mV. C) Normalized peak photocurrent as a function of 488 nm illumination intensity. Blue: average of n = 3 cells at 37 ºC; purple: average of n = 2 cells at 22 ºC. D) CapChR2 opening and closing time constants as a function of 488 nm illumination intensity. Opening (circles) and closing (squares). Blue: average of n = 3 cells at 37 ºC; purple: average of n = 2 cells at 22 ºC. E) Photocurrent for CapChR2 in HEK293T cell as a function of holding voltage. Reversal potential was Vrev = 15 mV. Experiment at 22 ºC. F) Effect of 594 nm illumination on CaPChR2 gating. Illumination at 594 nm, 0.21 mW/mm^2 induced 8% photocurrent compared to illumination at 488 nm, 0.22 mW/mm^2. Co-illumination with 594 and 488 nm reduced photocurrent by 30 pA, or 9.6% relative to 488 nm alone. Experiment at 22 ºC. G) Protocol for simultaneous optogenetic activation of CaPChR2 and measurement of Ca^{2+} dynamics via fluorescence of FR-GECO1c. H) Example neuron showing expression of FR-GECO1c (red, left) and CapChR2-eGFP (green, right). Scale bars 20 μm. An astrocyte

also expresses CapChR2-eGFP on the lower left. I) Representative fluorescence responses of FR-GECO1c at the soma in neurons with and without expression of CapChR2. Experiment at 37 ºC. J) Maximum fluorescence responses of FR-GECO1c at soma in neurons with (n = 9 neurons) and without (n = 7 neurons) CapChR2 expression. Experiment at 37 ºC.

3.3.2 Targeted stimulation probes Ca^{2+} length constants

We then used targeted optogenetic stimulation of small segments of dendrites to probe Ca^{2+} transport (Figure 9A), again in the presence of 2 μM TTX. We used synchronous alternation of the illumination wavelength and the DMD patterns at 10 Hz to target the blue light to small dendritic patches and to provide wide-area orange illumination (Figure 9B). The camera was also triggered synchronously with the illumination patterns (Figure 9C). The 50 ms interval between blue stimulation epochs was shorter than the measured off-time of CapChR2, so this protocol gave a quasi-continuous photocurrent and near-simultaneous wide-field Ca^{2+} imaging at an effective rate of 10 Hz and 50% duty cycles for imaging and stimulation. The protocol also included some frames of orange-only illumination at the beginning, to provide a fluorescence baseline, and some frames of blue-only illumination at the end, to measure blue-excited FR-GECO1c fluorescence for post-measurement crosstalk correction.

For each cell, we selected 3 – 6 well-separated dendritic regions to stimulate simultaneously. These regions were far enough apart that their calcium responses did not overlap. The FR-GECO1c fluorescence initially rose at the stimulus locations, and then spread, reaching a steady state after ~1 s (Figure 9D,E, Supplementary Movies 1, 2). The steady-state Ca^{2+} distribution extended substantially beyond the stimulated zone, showing the diffusion of Ca^{2+} ions from the stimulation spot (Figure 9D). We fit the shape of the calcium concentration profile with an exponential decay, with a length constant ϕ. In control experiments with neurons expressing only FR-GECO1c, targeted blue stimulation did not evoke a detectable change in FR-GECO1c fluorescence (Figure 10).

We measured the length constants from 135 local stimulation spots over 12 neurons for multiple stimulation intensities (Figure 9F). There was more cell-to-cell variability in ϕ between neurons than between spots within the same neuron. We speculate that this difference may be due to cell-to-cell differences in expression of Ca^{2+}-transport proteins, leading to differences in efflux rate. The population-

average length constant was 5.8 ± 2.3 μm (mean ± s.d.), with cell-average length constants ranging from 3.7 ± 0.7 μm to 10.8 ± 2.7 μm. This result is broadly consistent with the simulation results of Biess and coworkers, who predicted a steady-state full-width at half-maximum (FWHM) of the Ca^{2+} signal of 5 μm, corresponding to an exponential decay length constant of 3.6 μm.[149]

We then varied the stimulation intensity from 0.07 to 0.86 mW/mm^2 to test for concentration dependence of Ca^{2+} transport (Figure 9G). Steady-state Ca^{2+} concentration increased with stimulation intensity, as expected, but when the spatial profiles were normalized to their respective peaks, they appeared to have similar length constant (Figure 9G inset). Comparisons between stimulus locations were complicated by the large cell-to-cell variations in ϕ, and also by the fact that there were uncontrolled variations in optogenetic stimulation strength between regions. This spot-to-spot variability came from variations in CapChR2 expression level and from variations in the membrane area underlying each stimulation spot.

We thus focused on within-spot relations between Ca^{2+} level and length constant. For each spot, we calculated a $\phi_{norm} = \phi/\langle\phi\rangle$, where $\langle\phi\rangle$ is the average across stimulation intensities of ϕ for that spot. We then plotted ϕ_{norm} vs. ΔF/F (Figure 9H). We did not observe a global trend. We then fit the slope of ϕ_{norm} vs. ΔF/F for each stimulation spot, and plotted a histogram of the slopes. This histogram was centered at zero. Together, these results establish that we did not detect a relationship between the amplitude of the local Ca^{2+} transient and the steady-state length constant.

We also asked whether the length constant depended on contour distance, *d*, from the soma (Figure 9I). To account for the cell-to-cell variability in ϕ, we separately fit a line to ϕ vs. *d* for each cell. Length constants were slightly shorter in more distal dendrites, with a median slope of -0.012 (dimensionless; quartiles = [-0.025, 0.0058]). For example, at a slope of -.01, the length constant would be 1 μm shorter at 100 μm from the soma than near the soma. This distance dependence is consistent with a membrane-based Ca^{2+} efflux mechanism: smaller-diameter dendrites have higher surface-to-volume ratio, leading to more rapid efflux and hence shorter length constants. Our measurements are qualitatively consistent with the results of Korkotian and Segal, who measured that under impulsive Ca^{2+} uncaging the half-decay lengths were 1.5 μm in “thick” and 1.2 μm in “thin” dendrites (definitions not specified).[150]

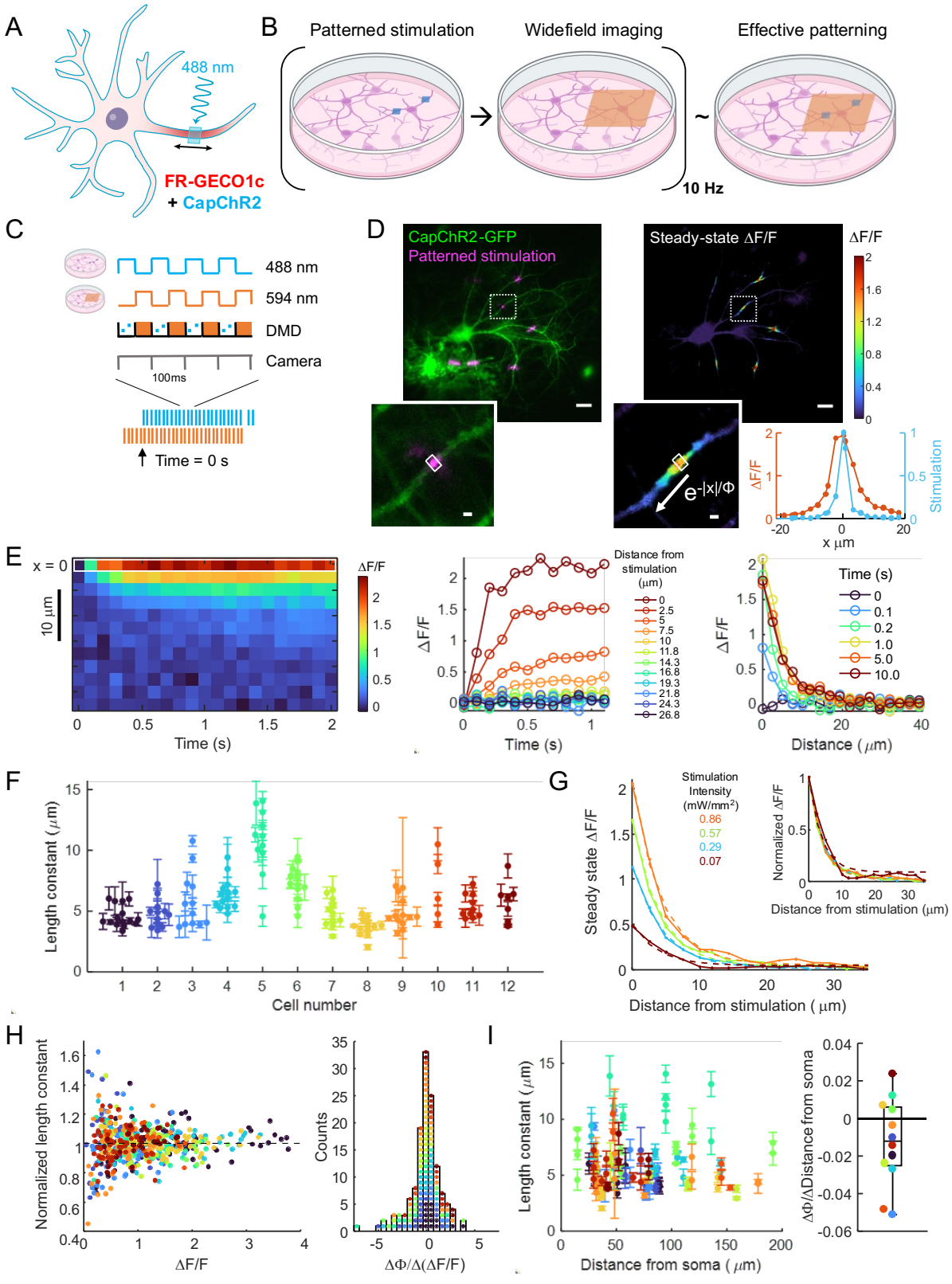

Figure 9: Measuring the Ca^{2+} length constant in dendrites.

A) Experimental scheme to test the spread of Ca^{2+} around a local optical stimulation of CapChR2. B) Rapid (10 Hz) alternation of targeted blue stimulation and wide-field orange illumination gave an effective pattern consisting of both. C) Experiment timing. Camera triggers were synchronized to acquire 1 frame per illumination cycle. 10 s of orange-only imaging at the start of the experiment provided a measure of baseline fluorescence. Blue light-evoked autofluorescence was measured at the end of the experiment. D) Top left: example neuron showing GFP fluorescence under wide-field illumination (indicative of CapChR2, green), and GFP fluorescence under patterned optogenetic stimulation (indicative of stimulus pattern, magenta). Top right: steady-state ΔF/F of FR-GECO1c. Insets show stimulated regions. Bottom right: profile of stimulation (eGFP fluorescence, blue) and steady-state ΔF/F of FR-GECO1c (orange). Top scale bars 20 μm, bottom scale bars 2 μm. E) Example response along a dendrite to localized stimulation. Left: Kymograph. Center: ΔF/F vs. time at different distances. Right: ΔF/F vs. position at different times. F) Length constants for multiple stimulation spots and multiple cells. Error bars show standard deviation of n = 3-5 measurements on same stimulation spot. G) Steady-state ΔF/F vs. distance from stimulation for experiments with varying stimulus intensities. Solid lines: data; dotted lines: exponential fits. Inset: plots normalized to their maximum ΔF/F. H) Left: length constant normalized by the average over multiple stimulation intensities at the same stimulation spot, colored by cell (n = 12 neurons, n = 135 stimulation spots). Peak ΔF/F was used as a proxy for local stimulation strength. For each stimulation spot, a line was fitted to the normalized length constant vs. peak ΔF/F. Right: histogram of slopes for these fits. I) Left: length constant at each stimulation spot vs. the contour distance from the soma, colored by cell. For each cell the data were fit to a line. Right: slopes of change in length constant vs. distance from soma.

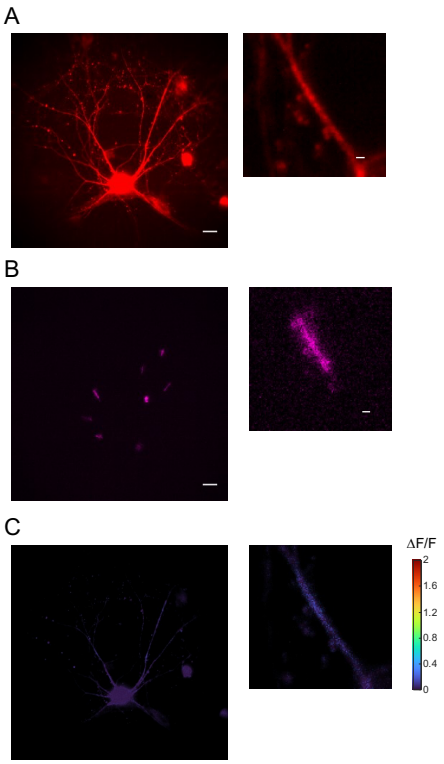

Figure 10: Effect of optical stimulation on neurons expressing sensor only.

A) FR-GECO1c expression of example cell (left, scale bar 20 μm) with zoom in on example dendrite (right, scale bar 2 μm). B) Local stimulation spots on example cell (left) with zoom in on example dendrite (right). C) Steady-State ΔF/F of example cell (left) with zoom in on example dendrite (right).

3.3.3 Wide-field stimulation probes Ca^{2+} dynamics

We used wide-field CapChR2 stimulation and wide-field FR-GECO1c imaging to map the cell-wide Ca^{2+} response kinetics to perturbations (Figure 11A). As before, we used TTX (2 μM) to suppress spiking. The stimulus waveform comprised three pulses of 6 s duration, with intensity increasing from 0.07 – 0.57 mW/mm^2, and with 20 s rest between pulses. At the end of the experiment, we turned off the orange light and recorded autofluorescence excited by the blue light alone for each stimulation intensity. These crosstalk signals were then subtracted from the data acquired with the orange laser on.

The cytosolic Ca^{2+} grew during each blue stimulus and returned toward baseline after, but the dynamics showed striking variations with distance from the soma (Figure 11B, C, Supplementary Movie 3). To quantify these dynamics, we defined several parameters, shown in Figure 11D. Figure 11E-H show maps of the Ca^{2+} dynamics for a representative neuron, and quantification of these dynamics as a function of distance from the soma. Upon stimulus onset, the fluorescence in distal branches peaked in $t_{max} < 1$ s and then started to decrease, whereas the fluorescence in the soma and nearby dendrites continued to grow for the full 6 s stimulus. The amount of sag in the fluorescence after the peak, $(\Delta F/F)_{sag}$, was greater in the distal branches than in and near the soma (where it was zero). Upon termination of the stimulus, the half-recovery time of the Ca^{2+} signal was faster in the distal dendrites ($t_{1/2} \sim 0.3$ s) than near the soma ($t_{1/2} \sim 0.6$ s). In the distal branches, the FR-GECO1c fluorescence then decreased below its initial basal value, before increasing back to baseline, while there was no fluorescence overshoot during recovery in and near the soma.

Figure 11I shows a summary of the proximal and distal recovery times across neurons and Figure 12 shows the distributions of the other kinetic parameters across cells. We defined the proximal dendrites to have $d < 20$ μm from the soma, and distal dendrites as $d > 60$ μm from the soma. As with the length constants, there was substantial cell-to-cell variability in the Ca^{2+} recovery kinetics, although the proximal-to-distal trends in the dynamics were consistent.

We propose that the proximal-to-distal variation in Ca^{2+} dynamics can be explained by the greater surface-to-volume ratio in the more distal dendrites[151,152]. For a given current density (influx or efflux) across the membrane, the rate of change of concentration in the dendrite scales as 1/*r*, where *r* is the radius of the dendrite. This scaling accounts for the shorter time to peak, t_{max}, in the smaller diameter distal dendrites. This scaling also likely accounts for the faster recovery time, $t_{1/2}$, in the more distal dendrites, where the efflux is through the Ca^{2+} ATP-ase (PMCA) and Na^{+}-Ca^{2+} Exchanger (NCX)[153].

The sag during the stimulus epoch and the post-stimulus overshoot cannot be explained within the linear reaction-diffusion model of Eq. 1. Since the sag and the overshoot colocalized within cells and co-varied in magnitude between cells, we propose that these are likely through a similar mechanism, e.g. a Ca^{2+} efflux mechanism that is activated at high Ca^{2+} concentration and remains active for a time after the Ca^{2+} concentration returns to baseline. We return to this mechanism in the next section.

The measurements of length constants (Figure 9) and recovery kinetics (Figure 11) were performed on the same cells, so we combined these measurements to estimate an effective diffusion coefficient, *D*. For each location where we had applied targeted stimulation and measured a length constant, we also determined the Ca^{2+} recovery time constant $t_{1/2}$ from the wide-field stimulation data. In a simple model of first-order efflux, the recovery rate constant is $k = \ln(2)\,/t_{1/2}$. While there was substantial cell-to-cell variation in ϕ (e.g. Figure 9D,F) and in $t_{1/2}$ (Figure 11G,I), on a log-log plot of ϕ vs. $t_{1/2}$, the data clustered along a line. The inferred effective diffusion coefficient was *D* =19.0 $\mu m^2/s$ (95 % Bootstrap Confidence Interval [16.9, 21.4], n = 8 neurons, 102 stimulation spots; Figure 11J,K).

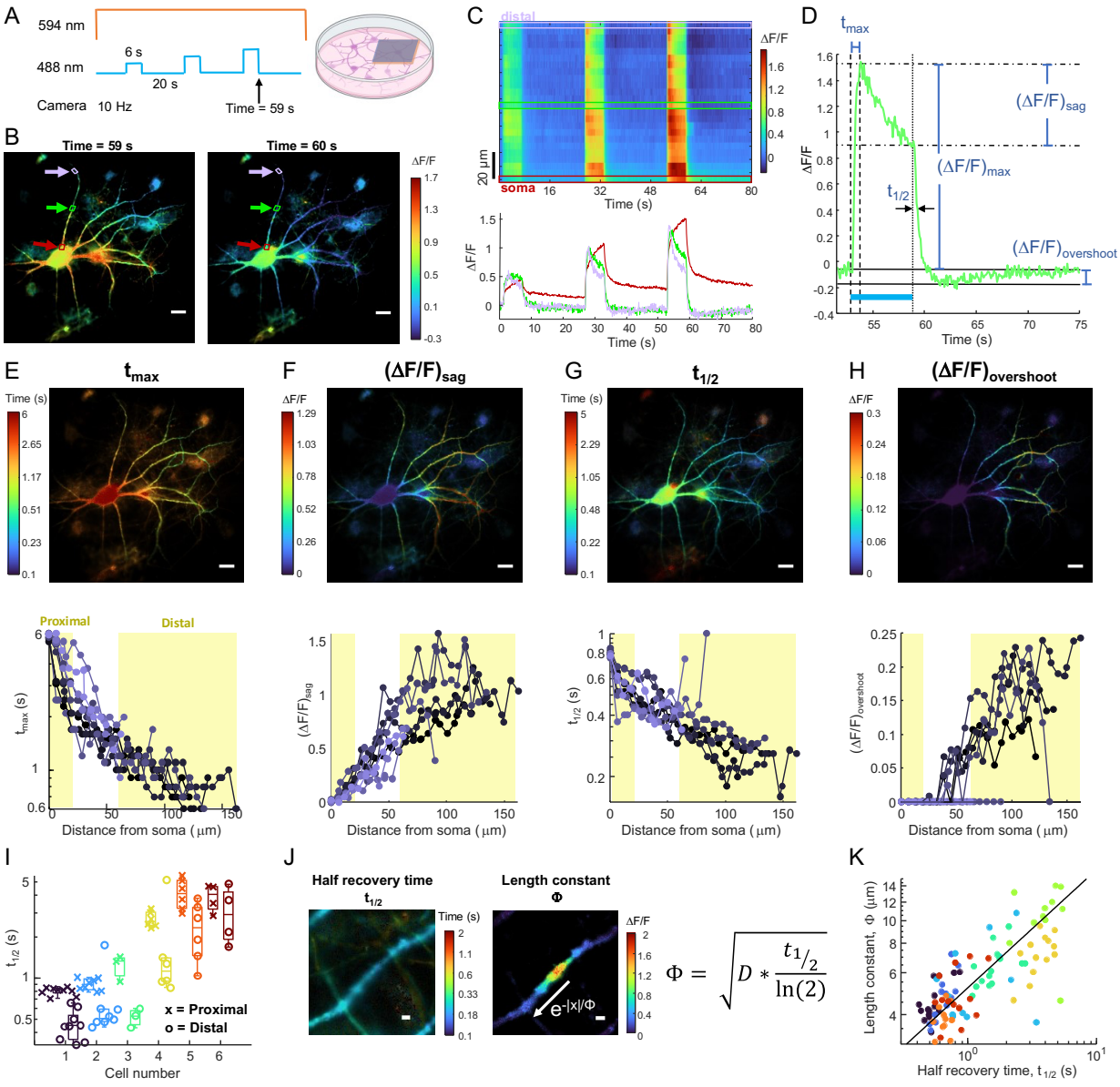

Figure 11: Ca^{2+} dynamics under wide-area stimulation.

A) Wide-area optogenetic stimulation induces global elevation in Ca^{2+}. B) Map of FR-GECO1c fluorescence. Left: at the end of the strongest stimulus pulse. Right: 1 s after the end of the stimulus. Scale bars 20 μm. C) Top: kymograph of ΔF/F (top) along dendrite shown by arrows in B. Bottom: fluorescence at locations marked by arrows in B. D) Example plot of ΔF/F showing the definitions of t_{max}, $(\Delta F/F)_{sag}$, $t_{1/2}$, and $(\Delta F/F)_{overshoot}$. E-H) Top: maps of the indicated kinetic parameters for a representative cell. Bottom: plotted as a function of contour distance from the soma. I) Indicated kinetic parameters averaged over proximal and distal dendrites across multiple cells. J) Left: map of the half recovery time, and right: the steady state ΔF/F in an example stimulation spot. Right: Predicted relation between recovery time, length constant, and diffusion coefficient. Scale bars 2 μm. K) Length constant, ϕ, vs. half-recovery time $t_{1/2}$. Median diffusion coefficient is shown as black line.

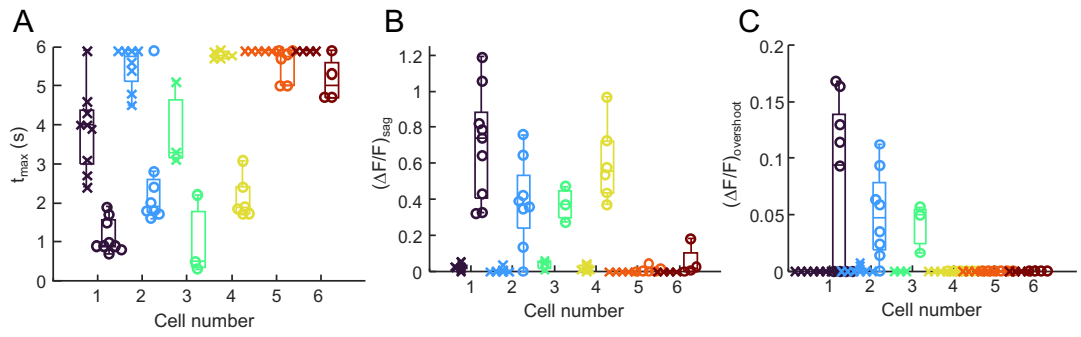

Figure 12: Cell-to-cell variability in parameters of Ca2+ dynamics.

A) t_{max} in proximal and distal dendrites across multiple cells. B) $(\Delta F/F)_{sag}$ in proximal and distal dendrites across multiple cells. C) $(\Delta F/F)_{overshoot}$ in proximal and distal dendrites across multiple cells.

3.3.4 NCX1 mediates nonlinear recovery kinetics

The sodium-calcium exchanger NCX1 is expressed in hippocampal pyramidal cell dendrites in vivo[154] and in culture.[155] NCX1 is a low-affinity (0.2 – 10 μM),[156] high-capacity electrogenic Ca^{2+} transporter, whose primary role is to mediate rapid efflux of Ca^{2+} following an action potential.[157] The activity of this antiporter is dynamically regulated by Ca^{2+} binding to allosteric regulatory sites, as well as by many other intracellular signals.[158] We thus hypothesized that the nonlinear dynamics in distal dendrites (sag during stimulation and overshoot following stimulation) might be attributable to Ca^{2+}-mediated allosteric enhancement of NCX1 activity.

We compared optogenetically evoked Ca^{2+} dynamics before and after blocking NCX1 with benzamil (30 μM; Figure 13A)[159]. In both proximal and distal dendrites, benzamil increased the time to maximum fluorescence, (t_{max}: 3.5 ± 1.7 s before, 4.1 ± 1.5 s after, P = 6.8e-8, paired two-sided t-test, n = 25 dendrites, 5 neurons), and increased the post-stimulation recovery time, ($t_{1/2}$: 1.8 ± 1.4 s before, 2.0 ± 1.4 s after, P = 1.8e-9, paired two-sided t-test). In distal dendrites, benzamil also decreased the sag during stimulation, ($(\Delta F/F)_{sag}$: 0.43 ± 0.27 before, 0.26 ± 0.23 after, P = 1.1e-9, paired two-sided t-test, n = 25 dendrites, 5 neurons), and largely eliminated the overshoot before return to baseline ($(\Delta F/F)_{overshoot}$: 0.058 ± 0.028 before, 0.034 ± 0.029 after, P = 0.0065, n = 12 dendrites, 3 neurons which displayed overshoot behavior before drug addition, paired two-sided t-test; Figure 13B). Together these results support the

hypothesis that NCX1 acts as a nonlinear efflux pump, activated at high Ca^{2+} and slowly inactivating upon return to baseline Ca^{2+}.

We did not observe an effect of benzamil on the length constant in either proximal or distal dendrites (Figure 13C). The measured increase in recovery time constant, $t_{1/2}$, was ~27%, implying an increase in length constant of ~13%. This change was likely too small for us to detect.

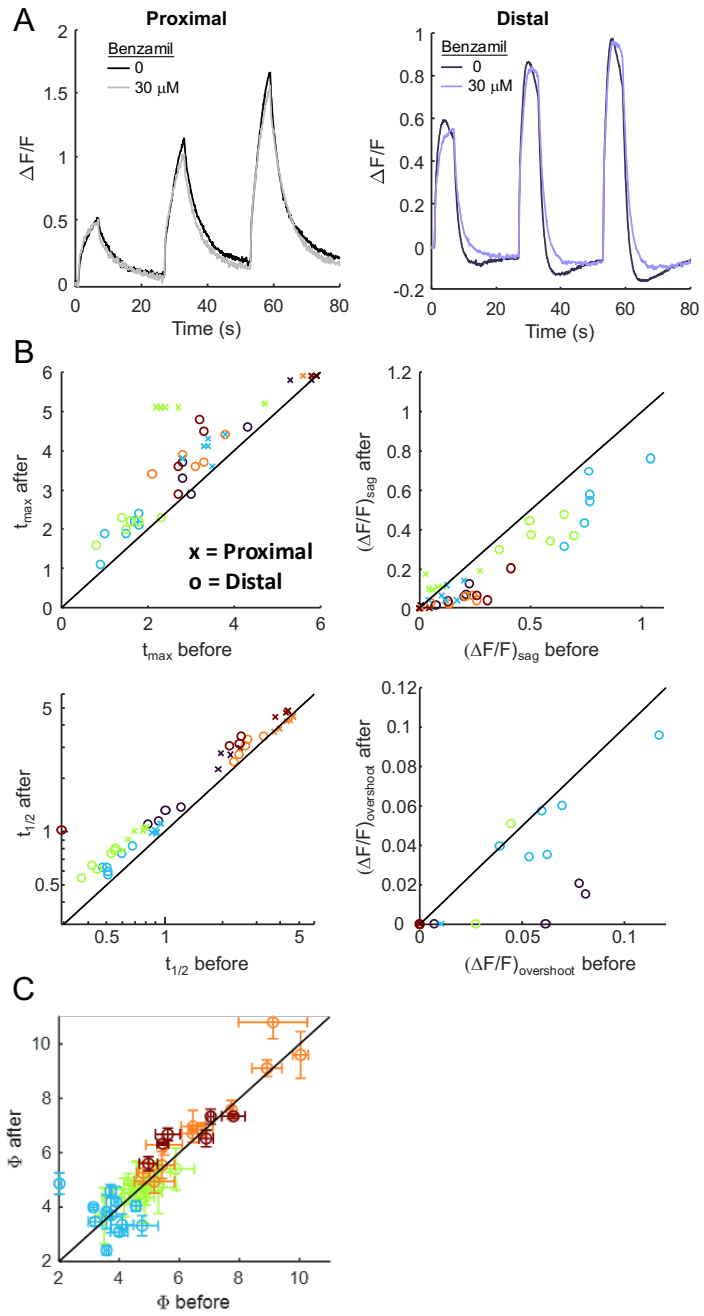

Figure 13: Effect of NCX block on calcium length constant and recovery kinetics.

A) Left: ΔF/F of proximal and right: distal section of example dendrite before (dark line) and after (light line) addition of benzamil to block NCX1. B) Effect of benzamil on t_{max} (top left), $(\Delta F/F)_{sag}$ (top right), $t_{1/2}$ (bottom left), and $(\Delta F/F)_{overshoot}$ (bottom right) in distal and proximal regions of dendrites (n = 25 dendrites, 5 neurons). C) Comparison of length constants (n = 41 dendrites, 4 neurons) before and after NCX1 block. Error bars show standard deviation over 3 measurements.

3.4 Discussion

We combined a blue-excited Ca^{2+}-permeable channelrhodopsin with an orange-excited fluorescent Ca^{2+} indicator for all-optical mapping of Ca^{2+} response-functions in dendrites. We measured length constants ϕ ~ 5.8 μm and recovery times $t_{1/2}$ ~ 1.7 s. From these, we calculated an effective Ca^{2+} diffusion coefficient, D ~20 $\mu m^2/s$. Though there was substantial branch-to-branch and cell-to-cell variation in ϕ and $t_{1/2}$, D was comparatively constant.

Free Ca^{2+} in water has a diffusion coefficient of D = 778 $\mu m^2/s$.[160] Several prior studies reported measurements of Ca^{2+} diffusion in cellular contexts. In a classic experiment in *Xenopus* egg extract, Allbritton, Meyer and Streyer measured a diffusion coefficient of 13 $\mu m^2/s$ for a radioactive $^{45}Ca^{2+}$ tracer at a basal concentration of 90 nM[141], which grew to 65 $\mu m^2/s$ at a basal concentration of 1 μM. However, in the Allbritton experiments, Ca^{2+} uptake and release from mitochondria and ER were pharmacologically blocked, so the roles of these stores on effective transport was not determined. A further critique of this result was that, by not mapping the concentration of the non-radioactive basal Ca^{2+} ions, the measurements ignored the contribution of these ions as they were displaced from buffers by $^{45}Ca^{2+}$ tracers, i.e. that “messages diffuse faster than the messenger”.[161] Also, in the long-and-thin geometry of dendrites, membranous organelles might occlude Ca^{2+} transport,[149] and dendritic spines might trap Ca^{2+} ions,[162] effects missing from purified cytoplasm. Despite these caveats, our results are broadly consistent with the results of Allbritton and coworkers, interpolated to a basal Ca^{2+} concentration of 100 – 200 nM.

More recent measurements used fluorescent Ca^{2+} indicators to measure transport of all Ca^{2+} ions. Murthy and coworkers measured the spread of Ca^{2+} signals in response to quantal activation of dendritic spines in cultured hippocampal pyramidal cells, and determined an effective diffusion coefficient of 21 $\mu m^2/s$ (95% CI: 10 – 36 $\mu m^2/s$),[140] remarkably close to our result. Biess and coworkers used photochemical uncaging of an inert dye to determine that geometrical effects alone (i.e. occlusion by organelles, trapping in spines, increased cytoplasmic viscosity) led to a ~20-fold decrease in D in hippocampal dendrites compared to free solution.[149] Thus, one would expect that once buffering is taken into account D_{Ca2+} < 778/20 = 39 $\mu m^2/s$ in dendrites. Noguchi and coworkers used two-photon glutamate uncaging and calcium imaging in rat CA1 pyramidal cells in acute hippocampal slices to estimate a length

constant of 1.6 – 1.9 μm and a calcium diffusion coefficient of 12 $\mu m^2/s$.[163] Korkotian and Segal used photochemical uncaging of Ca^{2+} directly in hippocampal dendrites and determined that Ca^{2+} transients spread over 3 – 3.5 μm, but did not extract a diffusion coefficient. A limitation of the above studies is that because they relied on an impulsive introduction of Ca^{2+} into the dendrite (either by synaptic input or by uncaging), it was difficult to distinguish between Ca^{2+} efflux and diffusion-driven dilution. This limitation may explain why other studies reported a modestly shorter length constant than we observed.

Using an analogous experiment with a blue-light activated adenylyl cyclase and a red-shifted cAMP reporter, we previously measured a dendritic length constant of cAMP transport ϕ_{cAMP} ~30 μm, and a dendritic diffusion coefficient of D_{cAMP} ~ 120 $\mu m^2/s$.[70] Allbritton and coworkers measured diffusion of inositol 1,4,5-trisphosphate (IP_3) in free cytosol and determined D_{IP3} ~ 283 $\mu m^2/s$. They estimated a range of action of ϕ_{IP3} ~ 24 μm, though both numbers would be expected to be smaller in dendrites due to the presence of occlusions and traps. Using a blue-light activated channelrhodopsin and a red-shifted voltage indicator, we previously measured a dendritic length constant of voltage transport ϕ_V ~255 μm.[137] This hierarchy of signaling length-scales is an important aspect of modeling neural dynamics.

Ca^{2+} handling differs between neuronal sub-types,[162,164–166], and is also fundamentally important in many non-neuronal cell types such as astrocytes[167], cardiomyocytes,[168] and immune cells.[169] Ca^{2+} signaling is also disrupted in many diseases of the nervous, cardiac, and immune systems. The tools we introduce here are expected to be compatible with a wide diversity of cell types. The tools could find application in high-throughput screens such as are used in drug development, in detailed mechanistic studies in cultured cells, and in applications in tissue and *in vivo*.

3.5 Materials and Methods

HEK293T cell culture: HEK293T cell lines were maintained at 37 °C, 5% CO_2 in Dulbecco's Modified Eagle Medium (DMEM) supplemented with 10% fetal bovine serum, 1% GlutaMax-I, penicillin (100 U/mL), streptomycin (100 μg/mL). For maintaining or expanding the cell culture, we used TC-treated

culture dishes (Corning). For all imaging experiments, cells were plated on poly-(D)-lysine (PDL)-coated glass-bottomed dishes (Cellvis, Cat.# D35-14-1.5-N).

Neuron culture: Primary E18 rat hippocampal neurons (fresh, never frozen, BrainBits #SDEHP) were dissociated following vendor protocols and plated in PDL-coated glass bottom dishes (Cellvis, Cat.# D35-14-1.5-N) at 21k/cm^2.

Cloning:

CAG-FR-GECO1c was a gift from Robert Campbell (Addgene plasmid # 163682) and CapChR2_pmScarlet-N1 was a gift from Peter Hegemann (Addgene plasmid # 188032). Each gene was cloned into a lentiviral backbone with CMV promoter and can be found on Addgene.

Lentivirus preparation: All lentivirus preparations were made in house. HEK293T cells were co-transfected with the second-generation packaging plasmid psPAX2 (Addgene #12260), envelope plasmid VSV-G (Addgene #12259) and transfer plasmids at a ratio of 9:4:14. For small batches of virus, we used 2.7 μg total plasmids and ~300k cells in 35-mm dish. Some viruses were concentrated 1:10 using Lenti-X Concentrator (Takara Cat. # 631232) following vendor protocols. Quantities of virus used are quoted using volumes prior to concentration.

Expression of optogenetic actuators and reporters: For characterization of CapChR2 photocurrents, HEK293T cells were transduced at least 2 days before imaging with 50-200 μL of lentivirus encoding CapChR2-eGFP.

Neurons were transduced after 6-10 days in culture with 200 μL lentivirus encoding FR-GECO1c driven by the CMV promoter and 50-200 μL of CapChR2-eGFP, also driven by the CMV promoter. Functional imaging was performed after 12-20 days in culture.

Sample preparation for imaging: Before optical stimulation and imaging, 35 mm dishes were washed with 1 mL PBS to remove residual culture medium, then filled with 2 mL extracellular (XC) buffer containing (in mM): 125 NaCl, 2.5 KCl, 2 $CaCl_2$, 1 $MgCl_2$, 15 HEPES, 25 glucose (pH 7.3). All imaging and electrophysiology were performed using this XC buffer. For all experiments in neurons, we added 10 μM

NBQX and 25 μM AP-V to block synaptic transmission, and 2 μM TTX to block spiking. For drug-addition experiments the stage-top incubator was briefly opened after the first imaging run for addition of 30 μM Benzamil (Tocris 3380) before commencing the second imaging run.

Electrophysiology: For patch clamp measurements, filamented glass micropipettes (WPI) were pulled to a resistance of 5–10 MΩ and filled with internal solution containing (in mM) 6 NaCl, 130 K-aspartate, 2 $MgCl_2$, 5 $CaCl_2$, 11 EGTA, and 10 HEPES (pH 7.2). The patch electrode was controlled with a low-noise patch clamp amplifier (Axon Instruments MultiClamp 700B). Current traces were collected in voltage clamp mode. The electrophysiology data were filtered with a moving average of 4 ms to reduce noise. The time constants were fit using single exponentials. In plots with multiple wavelengths of stimulation, the currents were normalized to the peak current for 488 nm stimulation.

Combined optogenetic stimulation and imaging: Experiments were conducted on a home-built inverted fluorescence microscope equipped with 488 nm and 594 nm laser lines and a scientific complementary metal-oxide semiconductor (CMOS) camera (Hamamatsu ORCA-Flash 4.0). Beams from both lasers were combined using dichroic mirrors and sent through an acousto-optic tunable filter (Gooch and Housego TF525-250-6-3-GH18A) for temporal modulation of intensity of each wavelength. The beams were then expanded and sent to a DMD (Vialux, V-7000 UV, 9515) for spatial modulation. The beams were focused onto the back-focal plane of a 60×/1.2-NA water-immersion objective (Olympus UIS2 UPlanSApo ×60/1.20W). Fluorescence emission was separated from laser excitation using a dichroic mirror (405/488/594). Imaging of FR-GECO1c fluorescence was performed with 594 nm laser at illumination intensity 0.21 mW/mm^2. Stimulation of CapChR2 was performed with 488 nm laser at illumination intensities of 0.005 - 1.5 mW/mm^2. Stimulation spots had lengths of 2-10 μm. Temperature was maintained using a covered stage-top incubator (Tokai Hit INUBG2ATFP-WSKM).

Data Analysis: All data were processed and analyzed in MATLAB. At the start of each measurement, prior to any optogenetic stimulation, the orange laser was turned on and the sample allowed to equilibrate for 5 s. Then baseline fluorescence, F_0, was measured via the average fluorescence during 4.5 s of 594 nm-only illumination. To correct for blue light-induced autofluorescence in the FR-GECO1c channel, at the end of the experiment images were acquired with blue-only illumination (orange light off). These

images were then subtracted from the corresponding frames acquired during simultaneous optogenetic stimulation and Ca^{2+} imaging.

Individual cells expressing the desired constructs were selected by hand and fluorescence waveforms were calculated by averaging pixels in the selected region and subtracting the background, which was computed by taking the 20th percentile of fluorescence intensity for pixels in a dark region of the field of view during imaging.

To determine steady-state Ca^{2+} length constant, the mean fluorescence profile was measured starting at the edge of the stimulation spot, from 6 - 19 s after blue stimulus onset. The profile was fit using a single exponential + constant.

To characterize the Ca^{2+} responses to wide-area stimulation, t_{max} was calculated as the time from the start of stimulation until maximum $\Delta F/F$. $(\Delta F/F)_{sag}$ was calculated as the difference between $\Delta F/F$ at t_{max} vs. at end of stimulation. $t_{1/2}$ was calculated as the time where $\Delta F/F$ was halfway between $\Delta F/F$ at the end of the stimulation and the baseline value after 20 s of relaxation. Linear interpolation was used to improve the time resolution in estimating $t_{1/2}$. $(\Delta F/F)_{overshoot}$ was calculated as the difference between the minimum of $\Delta F/F$ during the recovery phase and the $\Delta F/F$ baseline after smoothing with a gaussian-weighted average over 4 s windows. $(\Delta F/F)_{overshoot}$ was only accepted as genuine if it was larger than the standard deviation in the $\Delta F/F$ baseline. Proximal and Distal measurements were calculated by averaging the $\Delta F/F$ from all regions 0 – 20 μm from soma and beyond 60 μm from soma, respectively.

For measurements of Ca^{2+} dynamics before and after addition of benzamil, some acquisitions had small movements between the two sets of measurements. The raw data were aligned using image registration functions in Matlab to ensure the same spatial regions are used pre- and post-drug.

Chapter 4 Conclusion

This Dissertation explores the utility of all-optical systems for high spatial and kinetic control and measurement of ionic signaling. Here we focus on protons (Chapter 2) and calcium (Chapter 3). These ions have well-developed sensors for which we can focus on creating protocols and workflows. In Chapter 1 I motivated this work by examining the basis and importance of cellular signaling, the interests and concerns for signaling in neurons specifically, and the benefits of all-optical systems.

In Chapter 2 I looked at the channelrhodopsin CheRiff and measure the pH changes due to repeated stimulation, identifying the acidification as proton flux through the channelrhodopsin itself. I then characterized two new opsins and showed that they have low proton permeability, and can be used to eliminate acidification artifacts. This work shows the importance of choosing the right opsin, or, more generally, optogenetic actuator, for the specific use case and ensuring that it is functioning as intended.

In Chapter 3 I combined the optogenetic actuator CapChR2 for perturbing Ca^{2+} with the fluorescent Ca^{2+} indicator FR-GECO1c for all optical perturbation and measurement of Ca^{2+} in neurons. Using optical spatial patterning I created source points of Ca^{2+} in dendrites to image the spread of Ca^{2+} through the dendrite and measure the steady state spatial profile of a small local Ca^{2+} perturbation. These experiments gave an average length constant of Ca^{2+} in dendrites of 5.8 μm. I then used a short widefield perturbation to Ca^{2+} to map the recovery response of neurons to Ca^{2+} perturbations, giving an average recovery time of 1.7 s. Paired measurements of these parameters gave a diffusion coefficient of ~20 $\mu m^2/s$.

In this Chapter I first explore other possible combinations of optogenetic pairs for studying signaling pathways, as well as the strategies and factors for creating an optogenetic system. I then discuss some of the potential uses of all-optical systems in drug development.

4.1 Other optogenetic pairs

With the advance of optogenetics there are now many tools for modulation and sensing of different molecules, pathways, or physiological systems. These tools cross different spectral and kinetic ranges.

Many studies of signaling would benefit from the combined use of optogenetic control and monitoring tools. However, choosing which tools to use is complex, and requires understanding the optogenetic tools individually as well as how they will work together.

4.1.1 Spectral compatibility

The first step in creating an all-optical system is choosing a sensor and actuator that do not have spectral overlap. There are now red- and blue-shifted versions of many sensors and some actuators. It is often useful to combine a blue shifted actuator with a red shifted reporter, as it is generally less likely that red light will activate a blue shifted opsin than vice versa. Spurious excitation of the sensor by light intended for the actuator can be measured and controlled for in data analysis; but it is important that the system is not accidentally perturbed by spurious excitation of the actuator by light intended for the reporter. Such actuation could perturb the system in a way that may confuse the results. In addition, red shifted sensors can give better depth penetration for better imaging into tissues[170].

All-optical schemes must often take into account the complex photocycles of the actuator and reporter. It is important to check the combination of multiple wavelengths at the experimentally relevant intensities on the actuator and sensor individually, as the combination of multiple wavelengths can have unexpected effects. For example, red light shining on a blue shifted opsin during a bout of blue stimulation can close the opsin[111,112]. Sensors can also have activation from stimulation light. This can be controlled for by measuring the fluorescence from the stimulation light alone and subtracting it out of the data recorded during bouts of stimulation.

Non-linear effects of multiple wavelengths on the sample can be measured by using samples with only the sensor (no actuator) to repeat the experimental protocol and ensure that any stimulation light is not causing changes in fluorescence. This also checks for the stability in the sensor fluorescence over time, to control for changes in the sensor baseline during a measurement. Testing the response of the actuator to imaging light and the desired experimental protocol can be harder, depending on the signal being measured. For actuators which cause a change in the membrane potential via movement of ions across the membrane, patch clamp electrophysiology can be used to establish the sensor activation response. An alternative to having multiple wavelengths on at the same time is to use an optical switching scheme

in which the different wavelengths of light are not on at the same time, but are instead quickly switched on and off, as shown in (Chapter 3, Figure 9). This optical switching still requires some checks for controls such as the actuator response to imaging light as well as the stability of the sensor during experimental timelines.

4.1.2 Kinetic compatibility

Kinetics of sensors and actuators need to be compared to the temporal range of the signaling of interest. To ensure that the dynamics imaged accurately reflect the dynamics in signaling, the sensor used must have faster kinetics than the signal of interest. If the sensor response is slower than the signal, the kinetics will be blurred. Slow sensors can still be used for measurements of steady-state spatial profiles. A steady-state measurement of the spatial profile can tell you the maximum spread as shown in (Chapter 3, Figure 9). The sensor can also be viewed as an integrator of activity to show the possible spread over space for short perturbations without giving accurate timing measurements.

The kinetics of the actuator are important for determining the types of perturbations that can be created and how naturalistic these perturbations are. Knowledge of the actuator kinetics can be used to design optimal optical stimulation patterns. For example, to achieve long-term continuous stimulation, actuators with long off times will require lower total optical dose compared to actuators with short off times. This can be desirable, if photobleaching or phototoxicity are concerns. Step-function opsins have been created specifically for applications of long term continuous stimulation, as they require a short stimulation to turn on, and then they stay on until a different wavelength stimulation is used to turn them off[111,171]. While it can be useful for optogenetic actuators to replicate native signaling conditions, using these tools for stimulation with non-native patterns is also useful for exploring the response-properties of the system and for detailed biophysical modeling.

4.1.3 Signaling Pathways of interest

Many signaling pathways now have actuators and reporters that could be used for all-optical measurements. Here I illustrate three signaling systems: GPCR Gαq and RTKs through PLCγ, GPCR Gαs through adenylyl cyclases (ACs), and Mitochondria. Table 2 shows optical actuators that have interesting signals and the measured optical excitation peak wavelength. Table 3 shows some possible

sensors for the same signaling modalities which could potentially be combined with the actuators from Table 2 to create all-optical systems.

GPCR Gq and RTKs activate PLCγ, which takes phosphatidylinositol 4,5-bisphosphate (PIP_2) and makes diacylglycerol (DAG) and inositol trisphosphate (IP_3), which are small molecules in the membrane and cytosol, respectively. Because of the importance of GPCRs and RTKs and the large number of types of these receptors, there are many different existing optical actuators for these receptors. It is currently supposed that signaling specificity is at least partly due to the localization of the receptors inside the cell[74,172], however it would be interesting to test this hypothesis by directly stimulating receptors and imaging their signaling.

Another interesting measurement would be to look at the spread of IP_3 in neurons. It has been proposed that Ca^{2+} waves in neuronal dendrites are due to Ca^{2+} release from IP_3Rs in the S/ER. This release is triggered by IP_3, which can diffuse farther than Ca^{2+} in the cytoplasm[173,174]. However, there is debate about what the diffusion coefficient of IP_3 is[175,176] and if it is involved in Ca^{2+} waves. Currently, all measurements to estimate IP_3 diffusion have been measuring the downstream Ca^{2+} response, and not IP_3 itself. The combination of these actuators and reporters, for example neuropsin and IRIS, respectively, would give the ability to do a direct measurement of IP_3 spread and diffusion.

Signal	Actuators	Excitation (nm)	Notes	Addgene	Refs
GPCR Gαq and RTK through PLCγ	Opto- α1-adrenergic (A1AR)	500		20947, 106064	[177,178,179]
	Opto- α2-adrenergic (A2AR)			106066	[178,180]
	Neuropsin (Opn5)	405	no activation at 488, inactivated by 500	66460	[181,182]
	Melanopsin (Opn4)	488	inactivated by yellow, also signals through Gi/o	122630	[183,184,185]
	Opto-FGFR	488			[186,187]
GPCR Gαs through cAMP	Crblue	488		62917, 64204	[184]
	Opto- β2-adrenergic	500		20948, 106063	[177,178,188,189]

Mitochondria	mtOn	580	broad excitation		[190,191]
	mtOff	580	same as mtOn but in opposite direction		[192]
	mitoChR2	480	alters mito mem potential		[193,191]

Table 2: Table of optogenetic actuators for different signaling systems

Signal	Molecule	Sensor	Excitation (nm)	Emission (nm)	Sensor Mechanism	Addgene	Refs
GPCR Gq and RTK through PLCg	**IP3**	IRIS2	480	510/565	FRET		[194]
		fretino	440	480/535	FRET		[195]
		LIBRA	425	480/535	FRET		[196,197]
	DAG	Green/Red Upward/Downward DAG	506,590	517,600	FP	Montana Molecular Assay Kit	[198,199]
		C1AC1A	380	510	translocation of FP	61155	[200]
GPCR Gs through cAMP	**cAMP**	Pink Flamindo	567	590	FP	102356, 204669	[70,201]
		R-Flinca	571	590	FP		[202]
	PKA	ExRai-AKAR2	405/488	530	Excitation Ratiometric	161753	[203]
Mitochondria	**ATP**	ATPSnFR	490	512	FP	102549, 102550, 102556	[204]
		Queen	405	494	FP		[205]
		MaLionR, G, B	565,505,373	585,522,446	FP	113908, 113906, 113910	[206]
	ATP/ADP ratio	Perceval	430/490	530	FP	49082, 49083	[207,208]

Table 3: Table of optogenetic sensors for different signaling systems

4.2 Applications for drug development

While optogenetic studies have been interesting for understanding signaling in basic research, we believe all-optical studies could also be useful in drug development. As mentioned in Chapter 1, many diseases are due to improper signaling. Understanding signaling in health and disease will be helpful for finding drug targets and in characterizing candidate therapeutics. Additionally, the ability to investigate signaling

can be very helpful for the investigation of off-target effects of drugs, to ensure there isn't cross talk of drugs into other cellular functions that may cause toxicity.

4.2.1 Drug Screening

Within drug screening, one of the goals is to screen as many compounds as quickly and cheaply as possible, to have a better chance of finding new drug candidates. Optical stimulation reduces the need for consumable chemicals and reduces the time to take a measurement as the system can be directly and quickly stimulated. LEDs can be very cheap and can replace chemical stimuli. Optical stimulation is generally reversible and repeatable, which can help with the speed of testing by being able to quickly and effectively change stimulation patterns. The control of the optical elements also gives the ability to stimulate at different optical intensities, which can activate the optogenetic actuator to different degrees. Screening can then be easily done across various activations to explore state-dependent pharmacology in a fast high-throughput way. The repeatability of these measurements also gives the ability to do these repeat measurements in the same sample, to be able to look at changes in a specific cell and remove effects of cellular heterogeneity. As seen in Chapter 3 Figure 13, the cellular heterogeneity of the responses to stimulation can be much greater than the changes due to addition of drugs. Paired measurements in the same sample give the ability to see subtle changes.

The genetic targeting of optogenetic tools also gives the ability to use co-cultures where multiple cell types can be combined to make a more biologically relevant system, but still have the stimulation and measurement be in one specific subpopulation. Stimulation and imaging can even be targeted to separate cell-types for imaging effects of communication between two separate cell types and the effects they have on each other[209].

Optogenetics has started to be used for screening, such as investigating NaV[113], CaV and CNG[210], and RTK[211] signaling. As the optogenetic tools become better understood, and more reliable consistent protocols are developed, I believe the use of optogenetics in drug screening efforts will expand.

4.2.2 Hit testing

After screening has identified some compounds that show promise, hits are moved on to more in-depth analysis. This consists of studies on absorption, distribution, metabolism, and excretion (ADME) as well as studies on toxicity of the chosen hits. The versatility of fluorescent proteins is beneficial for these tests, especially as fluorescence imaging is a cheap and fast way to do testing, as discussed previously. Fluorescent reporters exist for many different molecules and cell states of interest, enabling the testing of many different effects. Optogenetic actuators can be combined with these sensors to look at the response to many different dynamic processes, which adds to the realism of the tests. For example, cardiotoxicity screening has been done using ChR for heart rate stimulation of cardiomyocytes[212].

4.2.3 Challenges

Some of the challenges with using optogenetics in drug development applications are the need for quantification of optogenetic stimulation which gives the need for good controls and experimental design, and the high quantity of data generated by high spatiotemporal resolution data.

In all-optical methods, stimulation using un-physiological systems may create perturbations outside of physiological regimes. Also, reporters show relative changes and not quantifications. These concerns can be mitigated by using good control experiments and experimental design. In systems in which the baseline is stable and predictable, the relative changes in fluorescence of the sensor can be used to find the real changes in the quantity being measured, via reference to standard calibration curves. We did this with pH in Chapter 2. In other systems, control experiments can be done using physiological stimuli or known perturbations which can give the maximum and minimum activation of the system. Bounds established by these measurements can be used to interpolate quantitative signals, such as done in [70].

Imaging over space and time gives 2 more axes of data which dramatically increases the amount of data produced by an experiment. This is part of what makes these measurements so rich in information, but the storage and analyses of this data can be a challenge. With the advances in technology and algorithms there are more abilities and techniques for storing and analyzing this data and for identifying subtle patterns.

References

1. Hayes, J. S., Brunton, L. L. & Mayer, S. E. Selective activation of particulate cAMP-dependent protein kinase by isoproterenol and prostaglandin E1. *J. Biol. Chem.* **255**, 5113–5119 (1980).
2. Brunton, L. L., Hayes, J. S. & Mayer, S. E. Hormonally specific phosphorylation of cardiac troponin I and activation of glycogen phosphorylase. *Nature* **280**, 78–80 (1979).
3. Mai, Q. N. *et al.* GPCR-dependent spatiotemporal cAMP generation confers functional specificity in cardiomyocytes and cardiac responses. 2022.07.13.499965 Preprint at https://doi.org/10.1101/2022.07.13.499965 (2022).
4. Ori, H. *et al.* Observation of topological action potentials in engineered tissues. *Nat. Phys.* **19**, 290–296 (2023).
5. Mylvaganam, S., Ramani, M., Krawczyk, M. & Carlen, P. L. Roles of gap junctions, connexins, and pannexins in epilepsy. *Front. Physiol.* **5**, (2014).
6. Dere, E. & Zlomuzica, A. The role of gap junctions in the brain in health and disease. *Neurosci. Biobehav. Rev.* **36**, 206–217 (2012).
7. Celesia, G. G. Disorders of membrane channels or channelopathies. *Clin. Neurophysiol.* **112**, 2–18 (2001).
8. Karpov, O. A. *et al.* Receptor tyrosine kinase structure and function in health and disease. *AIMS Biophys.* **2**, 476–502 (2015).
9. Heng, B. C., Aubel, D. & Fussenegger, M. An overview of the diverse roles of G-protein coupled receptors (GPCRs) in the pathophysiology of various human diseases. *Biotechnol. Adv.* **31**, 1676–1694 (2013).
10. Huang, Y., Todd, N. & Thathiah, A. The role of GPCRs in neurodegenerative diseases: avenues for therapeutic intervention. *Curr. Opin. Pharmacol.* **32**, 96–110 (2017).

11. SVOBODA, K. K. H. & REENSTRA, W. R. Approaches To Studying Cellular Signaling: A Primer For Morphologists. *Anat. Rec.* **269**, 123–139 (2002).
12. Almet, A. A., Cang, Z., Jin, S. & Nie, Q. The landscape of cell–cell communication through single-cell transcriptomics. *Curr. Opin. Syst. Biol.* **26**, 12–23 (2021).
13. Yan, G.-R. & He, Q.-Y. Functional proteomics to identify critical proteins in signal transduction pathways. *Amino Acids* **35**, 267–274 (2008).
14. Jun, J. J. *et al.* Fully integrated silicon probes for high-density recording of neural activity. *Nature* **551**, 232–236 (2017).
15. Reyes, A. D. A breakthrough method that became vital to neuroscience. *Nature* **575**, 38–39 (2019).
16. Reits, E. A. J. & Neefjes, J. J. From fixed to FRAP: measuring protein mobility and activity in living cells. *Nat. Cell Biol.* **3**, E145–E147 (2001).
17. Shrestha, D., Jenei, A., Nagy, P., Vereb, G. & Szöllősi, J. Understanding FRET as a Research Tool for Cellular Studies. *Int. J. Mol. Sci.* **16**, 6718–6756 (2015).
18. Cajal, S. R. y. *Cajal's Degeneration and Regeneration of the Nervous System*. (Oxford University Press, 1991).
19. Llinás, R. R. The contribution of Santiago Ramon y Cajal to functional neuroscience. *Nat. Rev. Neurosci.* **4**, 77–80 (2003).
20. Schuetze, S. M. The discovery of the action potential. *Trends Neurosci.* **6**, 164–168 (1983).
21. Bean, B. P. The action potential in mammalian central neurons. *Nat. Rev. Neurosci.* **8**, 451–465 (2007).
22. Wybo, W. A. M., Torben-Nielsen, B., Nevian, T. & Gewaltig, M.-O. Electrical Compartmentalization in Neurons. *Cell Rep.* **26**, 1759-1773.e7 (2019).

23. Ko, H. *et al.* The emergence of functional microcircuits in visual cortex. *Nature* **496**, 96–100 (2013).

24. Tononi, G., Sporns, O. & Edelman, G. M. A measure for brain complexity: relating functional segregation and integration in the nervous system. *Proc. Natl. Acad. Sci.* **91**, 5033–5037 (1994).

25. Jiruska, P. *et al.* Synchronization and desynchronization in epilepsy: controversies and hypotheses. *J. Physiol.* **591**, 787–797 (2013).

26. Zhou, X., Belavek, K. J. & Miller, E. W. Origins of Ca2+ imaging with fluorescent indicators. *Biochemistry* **60**, 3547–3554 (2021).

27. Grynkiewicz, G., Poenie, M. & Tsien, R. Y. A new generation of Ca2+ indicators with greatly improved fluorescence properties. *J. Biol. Chem.* **260**, 3440–3450 (1985).

28. Shimomura, O., Johnson, F. H. & Saiga, Y. Extraction, Purification and Properties of Aequorin, a Bioluminescent Protein from the Luminous Hydromedusan, Aequorea. *J. Cell. Comp. Physiol.* **59**, 223–239 (1962).

29. Hastings, J. W., Mitchell, G., Mattingly, P. H., Blinks, J. R. & Van Leeuwen, M. Response of Aequorin Bioluminescence to Rapid Changes in Calcium Concentration. *Nature* **222**, 1047–1050 (1969).

30. Miyawaki, A. *et al.* Fluorescent indicators for Ca2+based on green fluorescent proteins and calmodulin. *Nature* **388**, 882–887 (1997).

31. Chen, T.-W. *et al.* Ultrasensitive fluorescent proteins for imaging neuronal activity. *Nature* **499**, 295–300 (2013).

32. Zhao, Y. *et al.* An Expanded Palette of Genetically Encoded Ca2+ Indicators. *Science* **333**, 1888–1891 (2011).

33. Akerboom, J. *et al.* Genetically encoded calcium indicators for multi-color neural activity imaging and combination with optogenetics. *Front. Mol. Neurosci.* **6**, (2013).

34. Dalangin, R. *et al.* Far-red fluorescent genetically encoded calcium ion indicators. 2020.11.12.380089 Preprint at https://doi.org/10.1101/2020.11.12.380089 (2020).
35. Tian, W. *et al.* Dendritic Morphology Affects the Velocity and Amplitude of Back-propagating Action Potentials. *Neurosci. Bull.* **38**, 1330–1346 (2022).
36. Payeur, A., Béïque, J.-C. & Naud, R. Classes of dendritic information processing. *Curr. Opin. Neurobiol.* **58**, 78–85 (2019).
37. Larkum, M. E. Are Dendrites Conceptually Useful? *Neuroscience* **489**, 4–14 (2022).
38. Häusser, M. & Mel, B. Dendrites: bug or feature? *Curr. Opin. Neurobiol.* **13**, 372–383 (2003).
39. Urban, D. J. & Roth, B. L. DREADDs (designer receptors exclusively activated by designer drugs): chemogenetic tools with therapeutic utility. *Annu. Rev. Pharmacol. Toxicol.* **55**, 399–417 (2015).
40. Wang, S. S.-H., Khiroug, L. & Augustine, G. J. Quantification of spread of cerebellar long-term depression with chemical two-photon uncaging of glutamate. *Proc. Natl. Acad. Sci.* **97**, 8635–8640 (2000).
41. Zemelman, B. V., Nesnas, N., Lee, G. A. & Miesenböck, G. Photochemical gating of heterologous ion channels: Remote control over genetically designated populations of neurons. *Proc. Natl. Acad. Sci.* **100**, 1352–1357 (2003).
42. Boyden, E. S., Zhang, F., Bamberg, E., Nagel, G. & Deisseroth, K. Millisecond-timescale, genetically targeted optical control of neural activity. *Nat. Neurosci.* **8**, 1263–1268 (2005).
43. Jia, B. Z., Qi, Y., Wong-Campos, J. D., Megason, S. G. & Cohen, A. E. A bioelectrical phase transition patterns the first vertebrate heartbeats. *Nature* **622**, 149–155 (2023).
44. Liu, P. W. *et al.* A phenotypic screening platform for chronic pain therapeutics using all-optical electrophysiology. *PAIN* **165**, 922 (2024).
45. Córdova, C. *et al.* Optogenetic control of cancer cell survival in ChR2-transfected HeLa cells. *Int. J. Exp. Pathol.* **102**, 242–248 (2021).

46. Böhm, U. L. *et al.* Voltage imaging identifies spinal circuits that modulate locomotor adaptation in zebrafish. *Neuron* **110**, 1211-1222.e4 (2022).

47. Fan, L. Z. *et al.* All-Optical Electrophysiology Reveals the Role of Lateral Inhibition in Sensory Processing in Cortical Layer 1. *Cell* **180**, 521-535.e18 (2020).

48. Park, P. *et al.* Dendritic excitations govern back-propagation via a spike-rate accelerometer. 2023.06.02.543490 Preprint at https://doi.org/10.1101/2023.06.02.543490 (2024).

49. Tye, K. M. *et al.* Dopamine neurons modulate neural encoding and expression of depression-related behaviour. *Nature* **493**, 537–541 (2013).

50. Covington, H. E. *et al.* Antidepressant Effect of Optogenetic Stimulation of the Medial Prefrontal Cortex. *J. Neurosci.* **30**, 16082–16090 (2010).

51. Chen, B. T. *et al.* Rescuing cocaine-induced prefrontal cortex hypoactivity prevents compulsive cocaine seeking. *Nature* **496**, 359–362 (2013).

52. Gunaydin, L. A. *et al.* Natural Neural Projection Dynamics Underlying Social Behavior. *Cell* **157**, 1535–1551 (2014).

53. van Zessen, R., Phillips, J. L., Budygin, E. A. & Stuber, G. D. Activation of VTA GABA Neurons Disrupts Reward Consumption. *Neuron* **73**, 1184–1194 (2012).

54. Chow, B. Y. *et al.* High-performance genetically targetable optical neural silencing by light-driven proton pumps. *Nature* **463**, 98–102 (2010).

55. Zhang, F. *et al.* Multimodal fast optical interrogation of neural circuitry. *Nature* **446**, 633–639 (2007).

56. Mahn, M. *et al.* High-efficiency optogenetic silencing with soma-targeted anion-conducting channelrhodopsins. *Nat. Commun.* **9**, 4125 (2018).

57. Bernal Sierra, Y. A. *et al.* Potassium channel-based optogenetic silencing. *Nat. Commun.* **9**, 4611 (2018).

58. Sahel, J.-A. *et al.* Partial recovery of visual function in a blind patient after optogenetic therapy. *Nat. Med.* **27**, 1223–1229 (2021).

59. Bansal, A., Shikha, S. & Zhang, Y. Towards translational optogenetics. *Nat. Biomed. Eng.* **7**, 349–369 (2023).

60. Baleisyte, A., Schneggenburger, R. & Kochubey, O. Stimulation of medial amygdala GABA neurons with kinetically different channelrhodopsins yields opposite behavioral outcomes. *Cell Rep.* **39**, 110850 (2022).

61. Rickgauer, J. P., Deisseroth, K. & Tank, D. W. Simultaneous cellular-resolution optical perturbation and imaging of place cell firing fields. *Nat. Neurosci.* **17**, 1816–1824 (2014).

62. Packer, A. M., Russell, L. E., Dalgleish, H. W. P. & Häusser, M. Simultaneous all-optical manipulation and recording of neural circuit activity with cellular resolution in vivo. *Nat. Methods* **12**, 140–146 (2015).

63. Baker, C. A., Elyada, Y. M., Parra, A. & Bolton, M. M. Cellular resolution circuit mapping with temporal-focused excitation of soma-targeted channelrhodopsin. *eLife* **5**, e14193 (2016).

64. Stamatakis, A. M. *et al.* Simultaneous Optogenetics and Cellular Resolution Calcium Imaging During Active Behavior Using a Miniaturized Microscope. *Front. Neurosci.* **12**, 496 (2018).

65. Balachandar, L. *et al.* Simultaneous Ca2+ imaging and optogenetic stimulation of cortical astrocytes in adult murine brain slices. *Curr. Protoc. Neurosci.* **94**, e110 (2020).

66. Zhang, J. *et al.* All-optical imaging and patterned stimulation with a one-photon endoscope. 2021.12.19.473349 Preprint at https://doi.org/10.1101/2021.12.19.473349 (2022).

67. Hochbaum, D. R. *et al.* All-optical electrophysiology in mammalian neurons using engineered microbial rhodopsins. *Nat. Methods* **11**, 825–833 (2014).

68. Adam, Y. *et al.* Voltage imaging and optogenetics reveal behaviour-dependent changes in hippocampal dynamics. *Nature* **569**, 413 (2019).

69. Wong-Campos, J. D. *et al*. Voltage dynamics of dendritic integration and back-propagation in vivo. 2023.05.25.542363 Preprint at https://doi.org/10.1101/2023.05.25.542363 (2023).

70. Xiang, K. M., Park, P., Koren, S. A., Hayward, R. F. & Cohen, A. E. All-optical mapping of cAMP transport reveals rules of sub-cellular localization. 2023.06.27.546633 Preprint at https://doi.org/10.1101/2023.06.27.546633 (2023).

71. Stierl, M. *et al*. Light Modulation of Cellular cAMP by a Small Bacterial Photoactivated Adenylyl Cyclase, bPAC, of the Soil Bacterium Beggiatoa*♦. *J. Biol. Chem.* **286**, 1181–1188 (2011).

72. Harada, K. *et al*. Red fluorescent protein-based cAMP indicator applicable to optogenetics and in vivo imaging. *Sci. Rep.* **7**, 7351 (2017).

73. O'Banion, C. P., Vickerman, B. M., Haar, L. & Lawrence, D. S. Compartmentalized cAMP Generation by Engineered Photoactivated Adenylyl Cyclases. *Cell Chem. Biol.* **26**, 1393-1406.e7 (2019).

74. White, A. D. *et al*. Spatial bias in cAMP generation determines biological responses to PTH type 1 receptor activation. *Sci. Signal.* **14**, eabc5944 (2021).

75. Zaccolo, M. & Pozzan, T. Discrete Microdomains with High Concentration of cAMP in Stimulated Rat Neonatal Cardiac Myocytes. *Science* **295**, 1711–1715 (2002).

76. Bacskai, B. J. *et al*. Spatially Resolved Dynamics of cAMP and Protein Kinase A Subunits in Aplysia Sensory Neurons. *Science* **260**, 222–226 (1993).

77. Agarwal, S. R., Clancy, C. E. & Harvey, R. D. Mechanisms Restricting Diffusion of Intracellular cAMP. *Sci. Rep.* **6**, 19577 (2016).

78. Armingol, E., Officer, A., Harismendy, O. & Lewis, N. E. Deciphering cell–cell interactions and communication from gene expression. *Nat. Rev. Genet.* **22**, 71–88 (2021).

79. Davis, H. C. *et al*. Luminos. (2024).

80. Govorunova, E. G., Sineshchekov, O. A. & Spudich, J. L. Emerging Diversity of Channelrhodopsins and Their Structure-Function Relationships. *Front. Cell. Neurosci.* **15**, (2022).

81. Busskamp, V., Picaud, S., Sahel, J. A. & Roska, B. Optogenetic therapy for retinitis pigmentosa. *Gene Ther.* **19**, 169–175 (2012).

82. Sahel, J.-A. *et al.* Partial recovery of visual function in a blind patient after optogenetic therapy. *Nat. Med.* **27**, 1223–1229 (2021).

83. Chow, B. Y. & Boyden, E. S. Optogenetics and Translational Medicine. *Sci. Transl. Med.* **5**, 177ps5-177ps5 (2013).

84. Krook-Magnuson, E., Armstrong, C., Oijala, M. & Soltesz, I. On-demand optogenetic control of spontaneous seizures in temporal lobe epilepsy. *Nat. Commun.* **4**, 1376 (2013).

85. Bansal, A., Shikha, S. & Zhang, Y. Towards translational optogenetics. *Nat. Biomed. Eng.* 1–21 (2022) doi:10.1038/s41551-021-00829-3.

86. Beppu, K. *et al.* Optogenetic Countering of Glial Acidosis Suppresses Glial Glutamate Release and Ischemic Brain Damage. *Neuron* **81**, 314–320 (2014).

87. Bo, B., Li, Y., Li, W., Wang, Y. & Tong, S. Optogenetic translocation of protons out of penumbral neurons is protective in a rodent model of focal cerebral ischemia. *Brain Stimulat.* **13**, 881–890 (2020).

88. Nakao, S., Kojima, K. & Sudo, Y. Phototriggered Apoptotic Cell Death (PTA) Using the Light-Driven Outward Proton Pump Rhodopsin Archaerhodopsin-3. *J. Am. Chem. Soc.* **144**, 3771–3775 (2022).

89. Sinning, A. *et al.* Synaptic Glutamate Release Is Modulated by the Na+-Driven Cl−/HCO3− Exchanger Slc4a8. *J. Neurosci.* **31**, 7300–7311 (2011).

90. Xiang, Z.-M. & Bergold, P. J. Synaptic depression and neuronal loss in transiently acidic hippocampal slice cultures. *Brain Res.* **881**, 77–87 (2000).

91. Sinning, A. & Hübner, C. A. Minireview: pH and synaptic transmission. *FEBS Lett.* **587**, 1923–1928 (2013).

92. Lee, J., Taira, T., Pihlaja, P., Ransom, B. R. & Kaila, K. Effects of C02 on excitatory transmission apparently caused by changes in intracellular pH in the rat hippocampal slice. *Brain Res.* **706**, 210–216 (1996).

93. Dulla, C. G., Frenguelli, B. G., Staley, K. J. & Masino, S. A. Intracellular Acidification Causes Adenosine Release During States of Hyperexcitability in the Hippocampus. *J. Neurophysiol.* **102**, 1984–1993 (2009).

94. Cannizzaro, C., Monastero, R., Vacca, M. & Martire, M. [3H]-DA release evoked by low pH medium and internal H+ accumulation in rat hypothalamic synaptosomes: involvement of calcium ions. *Neurochem. Int.* **43**, 9–17 (2003).

95. Oginuma, M. *et al.* Intracellular pH controls WNT downstream of glycolysis in amniote embryos. *Nature* **584**, 98–101 (2020).

96. Fang, Y. *et al.* Smad5 acts as an intracellular pH messenger and maintains bioenergetic homeostasis. *Cell Res.* **27**, 1083–1099 (2017).

97. Lam, T. I. *et al.* Intracellular pH reduction prevents excitotoxic and ischemic neuronal death by inhibiting NADPH oxidase. *Proc. Natl. Acad. Sci.* **110**, E4362–E4368 (2013).

98. Shen, Y., Rosendale, M., Campbell, R. E. & Perrais, D. pHuji, a pH-sensitive red fluorescent protein for imaging of exo- and endocytosis. *J. Cell Biol.* **207**, 419–432 (2014).

99. Chen, F. *et al.* Visual function restoration with a highly sensitive and fast Channelrhodopsin in blind mice. *Signal Transduct. Target. Ther.* **7**, 1–3 (2022).

100. Hochbaum, D. R. *et al*. All-optical electrophysiology in mammalian neurons using engineered microbial rhodopsins. *Nat. Methods* **11**, 825–833 (2014).

101. Zhang, H., Reichert, E. & Cohen, A. E. Optical electrophysiology for probing function and pharmacology of voltage-gated ion channels. *eLife* **5**, e15202 (2016).

102. McNamara, H. M., Zhang, H., Werley, C. A. & Cohen, A. E. Optically controlled oscillators in an engineered bioelectric tissue. *Phys. Rev. X* **6**, 031001 (2016).

103. Werley, C. A., Chien, M.-P. & Cohen, A. E. Ultrawidefield microscope for high-speed fluorescence imaging and targeted optogenetic stimulation. *Biomed. Opt. Express* **8**, 5794–5813 (2017).

104. Wu, L., Dong, A., Dong, L., Wang, S.-Q. & Li, Y. PARIS, an optogenetic method for functionally mapping gap junctions. *eLife* **8**, e43366 (2019).

105. Huang, Y. L., Walker, A. S. & Miller, E. W. A photostable silicon rhodamine platform for optical voltage sensing. *J. Am. Chem. Soc.* **137**, 10767–10776 (2015).

106. Duan, X., Nagel, G. & Gao, S. Mutated Channelrhodopsins with Increased Sodium and Calcium Permeability. *Appl. Sci.* **9**, 664 (2019).

107. Vierock, J., Grimm, C., Nitzan, N. & Hegemann, P. Molecular determinants of proton selectivity and gating in the red-light activated channelrhodopsin Chrimson. *Sci. Rep.* **7**, 9928 (2017).

108. Hososhima, S., Shigemura, S., Kandori, H. & Tsunoda, S. P. Novel optogenetics tool: Gt_CCR4, a light-gated cation channel with high reactivity to weak light. *Biophys. Rev.* **12**, 453–459 (2020).

109. Scholz, N. *et al*. Mechano-dependent signaling by Latrophilin/CIRL quenches cAMP in proprioceptive neurons. *eLife* **6**, e28360 (2017).

110. Govorunova, E. G., Sineshchekov, O. A., Li, H., Janz, R. & Spudich, J. L. Characterization of a highly efficient blue-shifted channelrhodopsin from the marine alga Platymonas subcordiformis. *J. Biol. Chem.* **288**, 29911–29922 (2013).

111. Berndt, A., Yizhar, O., Gunaydin, L. A., Hegemann, P. & Deisseroth, K. Bi-stable neural state switches. *Nat. Neurosci.* **12**, 229–234 (2009).

112. Venkatachalam, V. *et al.* Flash memory: photochemical imprinting of neuronal action potentials onto a microbial rhodopsin. *J. Am. Chem. Soc.* **136**, 2529–2537 (2014).

113. Zhang, H., Reichert, E. & Cohen, A. E. Optical electrophysiology for probing function and pharmacology of voltage-gated ion channels. *eLife* **5**, e15202 (2016).

114. Wakabayashi, S., Shigekawa, M. & Pouyssegur, J. Molecular physiology of vertebrate Na+/H+ exchangers. *Physiol. Rev.* **77**, 51–74 (1997).

115. Hoffmann, E. K. & Simonsen, L. O. Membrane mechanisms in volume and pH regulation in vertebrate cells. *Physiol. Rev.* **69**, 315–382 (1989).

116. Chesler, M. & Kaila, K. Modulation of pH by neuronal activity. *Trends Neurosci.* **15**, 396–402 (1992).

117. Chesler, M. Regulation and Modulation of pH in the Brain. *Physiol. Rev.* **83**, 1183–1221 (2003).

118. Svichar, N., Esquenazi, S., Chen, H.-Y. & Chesler, M. Preemptive Regulation of Intracellular pH in Hippocampal Neurons by a Dual Mechanism of Depolarization-Induced Alkalinization. *J. Neurosci.* **31**, 6997–7004 (2011).

119. Ja, T., Rn, B., A, Z. & E, R. Intracellular pH measurements in Ehrlich ascites tumor cells utilizing spectroscopic probes generated in situ. *Biochemistry* **18**, (1979).

120. Miesenböck, G., De Angelis, D. A. & Rothman, J. E. Visualizing secretion and synaptic transmission with pH-sensitive green fluorescent proteins. *Nature* **394**, 192–195 (1998).

121. Werley, C. A., Chien, M.-P. & Cohen, A. E. Ultrawidefield microscope for high-speed fluorescence imaging and targeted optogenetic stimulation. *Biomed. Opt. Express* **8**, 5794–5813 (2017).

122. Clapham, D. E. Calcium Signaling. *Cell* **131**, 1047–1058 (2007).

123. Berchtold, M. W., Brinkmeier, H. & Müntener, M. Calcium Ion in Skeletal Muscle: Its Crucial Role for Muscle Function, Plasticity, and Disease. *Physiol. Rev.* **80**, 1215–1265 (2000).

124. Rubin, R. P. *Calcium and Cellular Secretion*. (Springer Science & Business Media, 2012).

125. Brini, M., Calì, T., Ottolini, D. & Carafoli, E. Neuronal calcium signaling: function and dysfunction. *Cell. Mol. Life Sci.* **71**, 2787–2814 (2014).

126. Blaustein, M. P. Calcium transport and buffering in neurons. *Trends Neurosci.* **11**, 438–443 (1988).

127. Augustine, G. J., Santamaria, F. & Tanaka, K. Local Calcium Signaling in Neurons. *Neuron* **40**, 331–346 (2003).

128. Heine, M., Heck, J., Ciuraszkiewicz, A. & Bikbaev, A. Dynamic compartmentalization of calcium channel signalling in neurons. *Neuropharmacology* **169**, 107556 (2020).

129. Gandini, M. A. & Zamponi, G. W. Voltage-gated calcium channel nanodomains: molecular composition and function. *FEBS J.* **289**, 614–633 (2022).

130. Berridge, M. J. Calcium microdomains: Organization and function. *Cell Calcium* **40**, 405–412 (2006).

131. Emptage, N. J., Reid, C. A. & Fine, A. Calcium Stores in Hippocampal Synaptic Boutons Mediate Short-Term Plasticity, Store-Operated Ca2+ Entry, and Spontaneous Transmitter Release. *Neuron* **29**, 197–208 (2001).

132. Sabatini, B. L., Maravall, M. & Svoboda, K. Ca2+ signaling in dendritic spines. *Curr. Opin. Neurobiol.* **11**, 349–356 (2001).

133. Delling, M., DeCaen, P. G., Doerner, J. F., Febvay, S. & Clapham, D. E. Primary cilia are specialized calcium signalling organelles. *Nature* **504**, 311–314 (2013).

134. Dittmer, P. J., Dell'Acqua, M. L. & Sather, W. A. Synaptic crosstalk conferred by a zone of differentially regulated Ca2+ signaling in the dendritic shaft adjoining a potentiated spine. *Proc. Natl. Acad. Sci.* **116**, 13611–13620 (2019).

135. Benedetti, L. *et al.* Periodic ER-plasma membrane junctions support long-range Ca2+ signal integration in dendrites. 2024.05.27.596121 Preprint at https://doi.org/10.1101/2024.05.27.596121 (2024).

136. Jia, B. Z., Qi, Y., Wong-Campos, J. D., Megason, S. G. & Cohen, A. E. A bioelectrical phase transition patterns the first vertebrate heartbeats. *Nature* **622**, 149–155 (2023).

137. Park, P. *et al.* Dendritic voltage imaging reveals biophysical basis of associative plasticity rules. 2023.06.02.543490 Preprint at https://doi.org/10.1101/2023.06.02.543490 (2023).

138. McNamara, H. M. *et al.* Optogenetic control of Nodal signaling patterns. 2024.04.11.588875 Preprint at https://doi.org/10.1101/2024.04.11.588875 (2024).

139. Fernandez Lahore, R. G. *et al.* Calcium-permeable channelrhodopsins for the photocontrol of calcium signalling. *Nat. Commun.* **13**, 7844 (2022).

140. Murthy, V. N., Sejnowski, T. J. & Stevens, C. F. Dynamics of dendritic calcium transients evoked by quantal release at excitatory hippocampal synapses. *Proc. Natl. Acad. Sci.* **97**, 901–906 (2000).

141. Allbritton, N. L., Meyer, T. & Stryer, L. Range of Messenger Action of Calcium Ion and Inositol 1,4,5-Trisphosphate. *Science* **258**, 1812–1815 (1992).

142. Wagner, J. & Keizer, J. Effects of rapid buffers on Ca2+ diffusion and Ca2+ oscillations. *Biophys. J.* **67**, 447–456 (1994).

143. Sandler, V. M. & Barbara, J.-G. Calcium-Induced Calcium Release Contributes to Action Potential-Evoked Calcium Transients in Hippocampal CA1 Pyramidal Neurons. *J. Neurosci.* **19**, 4325–4336 (1999).

144. Hausser, M., Spruston, N. & Stuart, G. J. Diversity and dynamics of dendritic signaling. *Science* **290**, 739–744 (2000).

145. Nicholls, D. G. Mitochondria and calcium signaling. *Cell Calcium* **38**, 311–317 (2005).

146. Frick, A. & Johnston, D. Plasticity of dendritic excitability. *J. Neurobiol.* **64**, 100–115 (2005).

147. Simons, S. B., Escobedo, Y., Yasuda, R. & Dudek, S. M. Regional differences in hippocampal calcium handling provide a cellular mechanism for limiting plasticity. *Proc. Natl. Acad. Sci.* **106**, 14080–14084 (2009).

148. Venkatachalam, V. & Cohen, A. E. Imaging GFP-based reporters in neurons with multiwavelength optogenetic control. *Biophys. J.* **107**, 1554–1563 (2014).

149. Biess, A., Korkotian, E. & Holcman, D. Barriers to Diffusion in Dendrites and Estimation of Calcium Spread Following Synaptic Inputs. *PLOS Comput. Biol.* **7**, e1002182 (2011).

150. Korkotian, E. & Segal, M. Spatially confined diffusion of calcium in dendrites of hippocampal neurons revealed by flash photolysis of caged calcium. *Cell Calcium* **40**, 441–449 (2006).

151. Holthoff, K., Tsay, D. & Yuste, R. Calcium Dynamics of Spines Depend on Their Dendritic Location. *Neuron* **33**, 425–437 (2002).

152. Cornelisse, L. N., Elburg, R. A. J. van, Meredith, R. M., Yuste, R. & Mansvelder, H. D. High Speed Two-Photon Imaging of Calcium Dynamics in Dendritic Spines: Consequences for Spine Calcium Kinetics and Buffer Capacity. *PLOS ONE* **2**, e1073 (2007).

153. Thayer, S. A., Usachev, Y. M. & Pottorf, W. J. Modulating Ca2+ clearance from neurons. *Front. Biosci.* **7**, d1255-79 (2002).

154. Minelli, A. *et al.* Cellular and subcellular localization of Na+–Ca2+ exchanger protein isoforms, NCX1, NCX2, and NCX3 in cerebral cortex and hippocampus of adult rat. *Cell Calcium* **41**, 221–234 (2007).

155. Thurneysen, T., Nicoll, D. A., Philipson, K. D. & Porzig, H. Sodium/calcium exchanger subtypes NCX1, NCX2 and NCX3 show cell-specific expression in rat hippocampus cultures. *Mol. Brain Res.* **107**, 145–156 (2002).

156. Giladi, M. & Khananshvili, D. Molecular Determinants of Allosteric Regulation in NCX Proteins. in *Sodium Calcium Exchange: A Growing Spectrum of Pathophysiological Implications: Proceedings of the 6th International Conference on Sodium Calcium Exchange* (ed. Annunziato, L.) 35–48 (Springer US, Boston, MA, 2013). doi:10.1007/978-1-4614-4756-6_4.

157. Khananshvili, D. Sodium-calcium exchangers (NCX): molecular hallmarks underlying the tissue-specific and systemic functions. *Pflüg. Arch. - Eur. J. Physiol.* **466**, 43–60 (2014).

158. Annunziato, L., Pignataro, G. & Molinaro, P. Na+/Ca2+ Exchangers. in *Encyclopedia of Molecular Pharmacology* (eds. Offermanns, S. & Rosenthal, W.) 1037–1047 (Springer International Publishing, Cham, 2021). doi:10.1007/978-3-030-57401-7_192.

159. Frelin, C. *et al.* Amiloride and its analogs as tools to inhibit Na+ transport *via* the Na+ channel, the Na+/H+ antiport and the Na+/Ca2+ exchanger. *Biochimie* **70**, 1285–1290 (1988).

160. Wang, J. H. Tracer-diffusion in Liquids. IV. Self-diffusion of Calcium Ion and Chloride Ion in Aqueous Calcium Chloride Solutions [1]. *J. Am. Chem. Soc.* **75**, 1769–1770 (1953).

161. Pando, B., Dawson, S. P., Mak, D.-O. D. & Pearson, J. E. Messages diffuse faster than messengers. *Proc. Natl. Acad. Sci.* **103**, 5338–5342 (2006).

162. Santamaria, F., Wils, S., De Schutter, E. & Augustine, G. J. Anomalous diffusion in Purkinje cell dendrites caused by spines. *Neuron* **52**, 635–648 (2006).

163. Noguchi, J., Matsuzaki, M., Ellis-Davies, G. C. R. & Kasai, H. Spine-Neck Geometry Determines NMDA Receptor-Dependent Ca2+ Signaling in Dendrites. *Neuron* **46**, 609–622 (2005).

164. Goldberg, J. H., Tamas, G., Aronov, D. & Yuste, R. Calcium Microdomains in Aspiny Dendrites. *Neuron* **40**, 807–821 (2003).

165. Goldberg, J. H., Yuste, R. & Tamas, G. Ca2+ imaging of mouse neocortical interneurone dendrites: Contribution of Ca2+-permeable AMPA and NMDA receptors to subthreshold Ca2+dynamics. *J. Physiol.* **551**, 67–78 (2003).

166. Soler-Llavina, G. J. & Sabatini, B. L. Synapse-specific plasticity and compartmentalized signaling in cerebellar stellate cells. *Nat. Neurosci.* **9**, 798–806 (2006).

167. Bazargani, N. & Attwell, D. Astrocyte calcium signaling: the third wave. *Nat. Neurosci.* **19**, 182–189 (2016).

168. Gilbert, G. *et al.* Calcium Signaling in Cardiomyocyte Function. *Cold Spring Harb. Perspect. Biol.* **12**, a035428 (2020).

169. Vig, M. & Kinet, J.-P. Calcium signaling in immune cells. *Nat. Immunol.* **10**, 21–27 (2009).

170. Yun, S. H. & Kwok, S. J. J. Light in diagnosis, therapy and surgery. *Nat. Biomed. Eng.* **1**, 1–16 (2017).

171. Brinks, D., Adam, Y., Kheifets, S. & Cohen, A. E. Painting with Rainbows: Patterning Light in Space, Time, and Wavelength for Multiphoton Optogenetic Sensing and Control. *Acc. Chem. Res.* **49**, 2518–2526 (2016).

172. Truong, M. E. *et al.* Vertebrate cells differentially interpret ciliary and extraciliary cAMP. *Cell* **184**, 2911-2926.e18 (2021).

173. Jaffe, L. F. Fast calcium waves. *Cell Calcium* **48**, 102–113 (2010).

174. Peercy, B. E. Initiation and propagation of a neuronal intracellular calcium wave. *J. Comput. Neurosci.* **25**, 334–348 (2008).

175. Dickinson, G. D., Ellefsen, K. L., Dawson, S. P., Pearson, J. E. & Parker, I. Hindered cytoplasmic diffusion of inositol trisphosphate restricts its cellular range of action. *Sci. Signal.* **9**, ra108–ra108 (2016).

176. Ornelas-Guevara, R., Gil, D., Voorsluijs, V. & Dupont, G. Computational investigation of IP3 diffusion. *Sci. Rep.* **13**, 2922 (2023).

177. Airan, R. D., Thompson, K. R., Fenno, L. E., Bernstein, H. & Deisseroth, K. Temporally precise in vivo control of intracellular signalling. *Nature* **458**, 1025–1029 (2009).

178. Morri, M. *et al.* Optical functionalization of human Class A orphan G-protein-coupled receptors. *Nat. Commun.* **9**, 1950 (2018).

179. Courtney, C. D. *et al.* Optoα1AR activation in astrocytes modulates basal hippocampal synaptic excitation and inhibition in a stimulation-specific manner. *Hippocampus* **33**, 1277–1291 (2023).

180. Li, P. *et al.* Optogenetic activation of intracellular adenosine A2A receptor signaling in the hippocampus is sufficient to trigger CREB phosphorylation and impair memory. *Mol. Psychiatry* **20**, 1339–1349 (2015).

181. Wagdi, A. *et al.* Selective optogenetic control of Gq signaling using human Neuropsin. *Nat. Commun.* **13**, 1765 (2022).

182. Leemann, S., Kleinlogel, S. & Schneider-Warme, F. Optogenetic interrogation of cell signalling: human neuropsin (hOPN5) represents a potent tool for controlling the Gq pathway with light. *Pflugers Arch.* **474**, 1217–1219 (2022).

183. Spoida, K. *et al.* Melanopsin Variants as Intrinsic Optogenetic On and Off Switches for Transient versus Sustained Activation of G Protein Pathways. *Curr. Biol. CB* **26**, 1206–1212 (2016).

184. Karunarathne, W. K. A., Giri, L., Kalyanaraman, V. & Gautam, N. Optically triggering spatiotemporally confined GPCR activity in a cell and programming neurite initiation and extension. *Proc. Natl. Acad. Sci.* **110**, E1565–E1574 (2013).

185. McGregor, K. M., Bécamel, C., Marin, P. & Andrade, R. Using melanopsin to study G protein signaling in cortical neurons. *J. Neurophysiol.* **116**, 1082–1092 (2016).

186. Kim, N., Kim, J. M. & Heo, W. D. Optogenetic Control of Fibroblast Growth Factor Receptor Signaling. *Methods Mol. Biol. Clifton NJ* **1408**, 345–362 (2016).

187. Kim, N. *et al.* Spatiotemporal control of fibroblast growth factor receptor signals by blue light. *Chem. Biol.* **21**, 903–912 (2014).

188. Siuda, E. R. *et al.* Optodynamic simulation of β-adrenergic receptor signalling. *Nat. Commun.* **6**, 8480 (2015).

189. Spangler, S. M. & Bruchas, M. R. Optogenetic approaches for dissecting neuromodulation and GPCR signaling in neural circuits. *Curr. Opin. Pharmacol.* **32**, 56–70 (2017).

190. Berry, B. J. *et al.* Optogenetic control of mitochondrial protonmotive force to impact cellular stress resistance. *EMBO Rep.* **21**, e49113 (2020).

191. Berry, B. J. & Wojtovich, A. P. Mitochondrial light switches: optogenetic approaches to control metabolism. *FEBS J.* **287**, 4544–4556 (2020).

192. Berry, B. J., Baldzizhar, A., Nieves, T. O. & Wojtovich, A. P. Neuronal AMPK coordinates mitochondrial energy sensing and hypoxia resistance in C. elegans. *FASEB J. Off. Publ. Fed. Am. Soc. Exp. Biol.* **34**, 16333–16347 (2020).

193. Tkatch, T. *et al.* Optogenetic control of mitochondrial metabolism and Ca2+ signaling by mitochondria-targeted opsins. *Proc. Natl. Acad. Sci.* **114**, E5167–E5176 (2017).

194. Matsu-ura, T. *et al.* Dual-FRET imaging of IP3 and Ca2+ revealed Ca2+-induced IP3 production maintains long lasting Ca2+ oscillations in fertilized mouse eggs. *Sci. Rep.* **9**, 4829 (2019).

195. Sato, M., Ueda, Y., Shibuya, M. & Umezawa, Y. Locating inositol 1,4,5-trisphosphate in the nucleus and neuronal dendrites with genetically encoded fluorescent indicators. *Anal. Chem.* **77**, 4751–4758 (2005).

196. Tanimura, A., Nezu, A., Morita, T., Turner, R. J. & Tojyo, Y. Fluorescent biosensor for quantitative real-time measurements of inositol 1,4,5-trisphosphate in single living cells. *J. Biol. Chem.* **279**, 38095–38098 (2004).

197. Tanimura, A. *et al.* Use of Fluorescence Resonance Energy Transfer-based Biosensors for the Quantitative Analysis of Inositol 1,4,5-Trisphosphate Dynamics in Calcium Oscillations. *J. Biol. Chem.* **284**, 8910–8917 (2009).

198. Tewson, P. *et al.* Simultaneous Detection of Ca2+ and Diacylglycerol Signaling in Living Cells. *PLOS ONE* **7**, e42791 (2012).

199. Werley, C. A., Boccardo, S., Rigamonti, A., Hansson, E. M. & Cohen, A. E. Multiplexed Optical Sensors in Arrayed Islands of Cells for multimodal recordings of cellular physiology. *Nat. Commun.* **11**, 3881 (2020).

200. Tsai, F.-C. *et al.* A polarized Ca2+, diacylglycerol and STIM1 signalling system regulates directed cell migration. *Nat. Cell Biol.* **16**, 133–144 (2014).

201. Harada, K. *et al.* Red fluorescent protein-based cAMP indicator applicable to optogenetics and in vivo imaging. *Sci. Rep.* **7**, 7351 (2017).

202. Ohta, Y., Furuta, T., Nagai, T. & Horikawa, K. Red fluorescent cAMP indicator with increased affinity and expanded dynamic range. *Sci. Rep.* **8**, 1866 (2018).

203. Zhang, J.-F. *et al.* An ultrasensitive biosensor for high-resolution kinase activity imaging in awake mice. *Nat. Chem. Biol.* **17**, 39–46 (2021).

204. Lobas, M. A. *et al.* A genetically encoded single-wavelength sensor for imaging cytosolic and cell surface ATP. *Nat. Commun.* **10**, 711 (2019).

205. Yaginuma, H. *et al.* Diversity in ATP concentrations in a single bacterial cell population revealed by quantitative single-cell imaging. *Sci. Rep.* **4**, 6522 (2014).

206. Arai, S. *et al.* RGB-Color Intensiometric Indicators to Visualize Spatiotemporal Dynamics of ATP in Single Cells. *Angew. Chem. Int. Ed.* **57**, 10873–10878 (2018).

207. Berg, J., Hung, Y. P. & Yellen, G. A genetically encoded fluorescent reporter of ATP:ADP ratio. *Nat. Methods* **6**, 161–166 (2009).

208. Tantama, M., Martínez-François, J. R., Mongeon, R. & Yellen, G. Imaging energy status in live cells with a fluorescent biosensor of the intracellular ATP-to-ADP ratio. *Nat. Commun.* **4**, 2550 (2013).

209. Fan, L. Z. *et al.* All-optical synaptic electrophysiology probes mechanism of ketamine-induced disinhibition. *Nat. Methods* **15**, 823–831 (2018).

210. Agus, V. *et al.* Bringing the light to High Throughput Screening: Use of optogenetic tools for the development of recombinant cellular assays. in vol. 9305 (2015).

211. Inglés-Prieto, Á. *et al.* Light-assisted small-molecule screening against protein kinases. *Nat. Chem. Biol.* **11**, 952–954 (2015).

212. Rehnelt, S. *et al.* Frequency-Dependent Multi-Well Cardiotoxicity Screening Enabled by Optogenetic Stimulation. *Int. J. Mol. Sci.* **18**, 2634 (2017).